

Fermi LAT observations of cosmic-ray electrons from 7 GeV to 1 TeV

M. Ackermann,¹ M. Ajello,¹ W. B. Atwood,² L. Baldini,³ J. Ballet,⁴ G. Barbiellini,^{5,6} D. Bastieri,^{7,8} B. M. Baughman,⁹ K. Bechtol,¹ F. Bellardi,³ R. Bellazzini,³ F. Belli,^{10,11} B. Berenji,¹ R. D. Blandford,¹ E. D. Bloom,¹ J. R. Bogart,¹ E. Bonamente,^{12,13} A. W. Borgland,¹ T. J. Brandt,^{14,9} J. Bregeon,³ A. Brez,³ M. Brigida,^{15,16} P. Bruel,¹⁷ R. Buehler,¹ T. H. Burnett,¹⁸ G. Busetto,^{7,8} S. Buson,^{7,8} G. A. Caliandro,¹⁹ R. A. Cameron,¹ P. A. Caraveo,²⁰ P. Carlson,^{21,22} S. Carrigan,⁸ J. M. Casandjian,⁴ M. Ceccanti,³ C. Cecchi,^{12,13} Ö. Çelik,^{23,24,25} E. Charles,¹ A. Chekhtman,^{26,27} C. C. Cheung,^{26,28} J. Chiang,¹ A. N. Cillis,^{29,23} S. Ciprini,¹³ R. Claus,¹ J. Cohen-Tanugi,³⁰ J. Conrad,^{31,22} R. Corbet,^{23,25} M. DeKlotz,³² C. D. Dermer,²⁶ A. de Angelis,³³ F. de Palma,^{15,16} S. W. Digel,¹ G. Di Bernardo,³ E. do Couto e Silva,¹ P. S. Drell,¹ A. Drlica-Wagner,¹ R. Dubois,¹ D. Fabiani,³ C. Favuzzi,^{15,16} S. J. Fegan,¹⁷ P. Fortin,¹⁷ Y. Fukazawa,³⁴ S. Funk,¹ P. Fusco,^{15,16} D. Gaggero,³ F. Gargano,¹⁶ D. Gasparrini,³⁵ N. Gehrels,²³ S. Germani,^{12,13} N. Giglietto,^{15,16} P. Giommi,³⁵ F. Giordano,^{15,16} M. Giroletti,³⁶ T. Glanzman,¹ G. Godfrey,¹ D. Grasso,³ I. A. Grenier,⁴ M.-H. Grondin,^{37,38} J. E. Grove,²⁶ S. Guiriec,³⁹ M. Gustafsson,⁷ D. Hadasch,⁴⁰ A. K. Harding,²³ M. Hayashida,¹ E. Hays,²³ D. Horan,¹⁷ R. E. Hughes,⁹ G. Jóhannesson,¹ A. S. Johnson,¹ R. P. Johnson,² W. N. Johnson,²⁶ T. Kamae,¹ H. Katagiri,³⁴ J. Kataoka,⁴¹ M. Kerr,¹⁸ J. Knödseder,¹⁴ M. Kuss,³ J. Lande,¹ L. Latronico,³ M. Lemoine-Goumard,^{37,38} M. Llana Garde,^{31,22} F. Longo,^{5,6} F. Loparco,^{15,16} B. Lott,^{37,38} M. N. Lovellette,²⁶ P. Lubrano,^{12,13} A. Makeev,^{26,27} M. N. Mazziotta,¹⁶ J. E. McEnery,^{23,42} J. Mehault,³⁰ P. F. Michelson,¹ M. Minuti,³ W. Mitthumsiri,¹ T. Mizuno,³⁴ A. A. Moiseev,^{24,42,*} C. Monte,^{15,16} M. E. Monzani,¹ E. Moretti,^{5,6} A. Morselli,¹⁰ I. V. Moskalenko,¹ S. Murgia,¹ T. Nakamori,⁴¹ M. Naumann-Godo,⁴ P. L. Nolan,¹ J. P. Norris,⁴³ E. Nuss,³⁰ T. Ohsugi,⁴⁴ A. Okumura,⁴⁵ N. Omodei,¹ E. Orlando,⁴⁶ J. F. Ormes,⁴³ M. Ozaki,⁴⁵ D. Paneque,¹ J. H. Panetta,¹ D. Parent,^{26,27} V. Pelassa,³⁰ M. Pepe,^{12,13} M. Pesce-Rollins,³ V. Petrosian,¹ M. Pinchera,³ F. Piron,³⁰ T. A. Porter,¹ S. Profumo,² S. Rainò,^{15,16} R. Rando,^{7,8} E. Rapposelli,³ M. Razzano,³ A. Reimer,^{47,1} O. Reimer,^{47,1} T. Reposeur,^{37,38} J. Ripken,^{31,22} S. Ritz,² L. S. Rochester,¹ R. W. Romani,¹ M. Roth,¹⁸ H. F.-W. Sadrozinski,² N. Saggini,³ D. Sanchez,¹⁷ A. Sander,⁹ C. Sgrò,^{3,†} E. J. Siskind,⁴⁸ P. D. Smith,⁹ G. Spandre,³ P. Spinelli,^{15,16} L. Stawarz,^{45,49} T. E. Stephens,^{23,50} M. S. Strickman,²⁶ A. W. Strong,⁴⁶ D. J. Suson,⁵¹ H. Tajima,¹ H. Takahashi,⁴⁴ T. Takahashi,⁴⁵ T. Tanaka,¹ J. B. Thayer,¹ J. G. Thayer,¹ D. J. Thompson,²³ L. Tibaldo,^{7,8,4} O. Tibolla,⁵² D. F. Torres,^{19,40} G. Tosti,^{12,13} A. Tramacere,^{1,53,54} M. Turri,¹ Y. Uchiyama,¹ T. L. Usher,¹ J. Vandenbroucke,¹ V. Vasileiou,^{24,25} N. Vilchez,¹⁴ V. Vitale,^{10,11} A. P. Waite,¹ E. Wallace,¹⁸ P. Wang,¹ B. L. Winer,⁹ K. S. Wood,²⁶ Z. Yang,^{31,22} T. Ylinen,^{21,55,22} and M. Ziegler²

(Fermi LAT Collaboration)

¹W. W. Hansen Experimental Physics Laboratory,
Kavli Institute for Particle Astrophysics and Cosmology,
Department of Physics and SLAC National Accelerator Laboratory,
Stanford University, Stanford, California 94305, USA

²Santa Cruz Institute for Particle Physics, Department of Physics and Department of Astronomy and Astrophysics,
University of California at Santa Cruz, Santa Cruz, California 95064, USA

³Istituto Nazionale di Fisica Nucleare, Sezione di Pisa, I-56127 Pisa, Italy

⁴Laboratoire AIM, CEA-IRFU/CNRS/Université Paris Diderot,
Service d'Astrophysique, CEA Saclay, 91191 Gif sur Yvette, France

⁵Istituto Nazionale di Fisica Nucleare, Sezione di Trieste, I-34127 Trieste, Italy

⁶Dipartimento di Fisica, Università di Trieste, I-34127 Trieste, Italy

⁷Istituto Nazionale di Fisica Nucleare, Sezione di Padova, I-35131 Padova, Italy

⁸Dipartimento di Fisica "G. Galilei", Università di Padova, I-35131 Padova, Italy

⁹Department of Physics, Center for Cosmology and Astro-Particle Physics,
The Ohio State University, Columbus, Ohio 43210, USA

¹⁰Istituto Nazionale di Fisica Nucleare, Sezione di Roma "Tor Vergata", I-00133 Roma, Italy

¹¹Dipartimento di Fisica, Università di Roma "Tor Vergata", I-00133 Roma, Italy

¹²Istituto Nazionale di Fisica Nucleare, Sezione di Perugia, I-06123 Perugia, Italy

¹³Dipartimento di Fisica, Università degli Studi di Perugia, I-06123 Perugia, Italy

¹⁴Centre d'Étude Spatiale des Rayonnements, CNRS/UPS, BP 44346, F-30128 Toulouse Cedex 4, France

¹⁵Dipartimento di Fisica "M. Merlin" dell'Università e del Politecnico di Bari, I-70126 Bari, Italy

¹⁶Istituto Nazionale di Fisica Nucleare, Sezione di Bari, 70126 Bari, Italy

¹⁷Laboratoire Leprince-Ringuet, École Polytechnique, CNRS/IN2P3, Palaiseau, France

¹⁸Department of Physics, University of Washington, Seattle, Washington 98195-1560, USA

¹⁹Institut de Ciències de l'Espai (IEEC-CSIC), Campus UAB, 08193 Barcelona, Spain

²⁰INAF-Istituto di Astrofisica Spaziale e Fisica Cosmica, I-20133 Milano, Italy

²¹Department of Physics, Royal Institute of Technology (KTH), AlbaNova, SE-106 91 Stockholm, Sweden

²²The Oskar Klein Centre for Cosmoparticle Physics, AlbaNova, SE-106 91 Stockholm, Sweden

- ²³NASA Goddard Space Flight Center, Greenbelt, Maryland 20771, USA
- ²⁴Center for Research and Exploration in Space Science and Technology (CRESST) and NASA Goddard Space Flight Center, Greenbelt, Maryland 20771, USA
- ²⁵Department of Physics and Center for Space Sciences and Technology, University of Maryland Baltimore County, Baltimore, Maryland 21250, USA
- ²⁶Space Science Division, Naval Research Laboratory, Washington, D. C. 20375, USA
- ²⁷George Mason University, Fairfax, Virginia 22030, USA
- ²⁸National Research Council Research Associate, National Academy of Sciences, Washington, D. C. 20001, USA
- ²⁹Instituto de Astronomía y Física del Espacio, Parbellón IAFE, Cdad. Universitaria, Buenos Aires, Argentina
- ³⁰Laboratoire de Physique Théorique et Astroparticules, Université Montpellier 2, CNRS/IN2P3, Montpellier, France
- ³¹Department of Physics, Stockholm University, AlbaNova, SE-106 91 Stockholm, Sweden
- ³²Stellar Solutions Inc., 250 Cambridge Avenue, Suite 204, Palo Alto, California 94306, USA
- ³³Dipartimento di Fisica, Università di Udine and Istituto Nazionale di Fisica Nucleare, Sezione di Trieste, Gruppo Collegato di Udine, I-33100 Udine, Italy
- ³⁴Department of Physical Sciences, Hiroshima University, Higashi-Hiroshima, Hiroshima 739-8526, Japan
- ³⁵Agenzia Spaziale Italiana (ASI) Science Data Center, I-00044 Frascati (Roma), Italy
- ³⁶INAF Istituto di Radioastronomia, 40129 Bologna, Italy
- ³⁷CNRS/IN2P3, Centre d'Études Nucléaires Bordeaux Gradignan, UMR 5797, Gradignan, 33175, France
- ³⁸Université de Bordeaux, Centre d'Études Nucléaires Bordeaux Gradignan, UMR 5797, Gradignan, 33175, France
- ³⁹Center for Space Plasma and Aeronomic Research (CSPAR), University of Alabama in Huntsville, Huntsville, Alabama 35899, USA
- ⁴⁰Institució Catalana de Recerca i Estudis Avançats (ICREA), Barcelona, Spain
- ⁴¹Research Institute for Science and Engineering, Waseda University, 3-4-1, Okubo, Shinjuku, Tokyo, 169-8555 Japan
- ⁴²Department of Physics and Department of Astronomy, University of Maryland, College Park, Maryland 20742, USA
- ⁴³Department of Physics and Astronomy, University of Denver, Denver, Colorado 80208, USA
- ⁴⁴Hiroshima Astrophysical Science Center, Hiroshima University, Higashi-Hiroshima, Hiroshima 739-8526, Japan
- ⁴⁵Institute of Space and Astronautical Science, JAXA, 3-1-1 Yoshinodai, Sagami-hara, Kanagawa 229-8510, Japan
- ⁴⁶Max-Planck Institut für extraterrestrische Physik, 85748 Garching, Germany
- ⁴⁷Institut für Astro- und Teilchenphysik and Institut für Theoretische Physik, Leopold-Franzens-Universität Innsbruck, A-6020 Innsbruck, Austria
- ⁴⁸NYCB Real-Time Computing Inc., Lattinotown, New York 11560-1025, USA
- ⁴⁹Astronomical Observatory, Jagiellonian University, 30-244 Kraków, Poland
- ⁵⁰Wyle Laboratories, El Segundo, California 90245-5023, USA
- ⁵¹Department of Chemistry and Physics, Purdue University Calumet, Hammond, Indiana 46323-2094, USA
- ⁵²Institut für Theoretische Physik and Astrophysik, Universität Würzburg, D-97074 Würzburg, Germany
- ⁵³Consorzio Interuniversitario per la Fisica Spaziale (CIFS), I-10133 Torino, Italy
- ⁵⁴INTEGRAL Science Data Centre, CH-1290 Versoix, Switzerland
- ⁵⁵School of Pure and Applied Natural Sciences, University of Kalmar, SE-391 82 Kalmar, Sweden

We present the results of our analysis of cosmic-ray electrons using about 8×10^6 electron candidates detected in the first 12 months on-orbit by the Fermi Large Area Telescope. This work extends our previously published cosmic-ray electron spectrum down to 7 GeV, giving a spectral range of approximately 2.5 decades up to 1 TeV. We describe in detail the analysis and its validation using beam-test and on-orbit data. In addition, we describe the spectrum measured via a subset of events selected for the best energy resolution as a cross-check on the measurement using the full event sample. Our electron spectrum can be described with a power law $\propto E^{-3.08 \pm 0.05}$ with no prominent spectral features within systematic uncertainties. Within the limits of our uncertainties, we can accommodate a slight spectral hardening at around 100 GeV and a slight softening above 500 GeV.

PACS numbers: 96.50.sb, 95.35.+d, 95.85.Ry, 98.70.Sa

I. INTRODUCTION

We report here a new analysis of our cosmic-ray electron (CRE, includes positrons) data sample, at energies between 7 GeV and 1 TeV based on measurements made using data from the first full year of on-orbit operations of the *Fermi* Gamma-ray Space Telescope's Large Area Tele-

*alexander.a.moiseev@nasa.gov

†carmelo.sgro@pi.infn.it

scope (LAT) [1]. Fermi was launched on June 11, 2008, into a circular orbit at 565 km altitude and 25.6° inclination. This paper extends the energy range of our previous measurement [2] down to 7 GeV, and provides more detailed information about our previous analysis based on the first six months of operations. In our earlier work, we reported that the CRE spectrum between 20 GeV and 1 TeV has a harder spectral index (best fit 3.04 in the case of a single power law) than previously indicated (in the range 3.1 to 3.4) [3–5], showing an excess of CREs at energies above 100 GeV with respect to most pre-Fermi experiments. The extension down to 7 GeV takes us close to the lowest geomagnetic cutoff energy accessible to the Fermi satellite. This part of the spectrum is important for understanding the heliospheric transport of CREs.

High-energy ($\gtrsim 100$ GeV) CREs lose their energy rapidly ($-dE/dt \propto E^2$) by synchrotron radiation on Galactic magnetic fields and by inverse Compton scattering on the interstellar radiation field. The typical distance over which a 1 TeV CRE loses half its total energy is estimated to be 300–400 pc (see e.g. [6]) when it propagates within about 1 kpc of the Sun. This makes them a unique tool for probing nearby Galactic space. Lower-energy CREs are affected more readily by energy-dependent diffusive losses, convective processes in the interstellar medium, and perhaps reacceleration by second-order Fermi processes during transport from their sources to us. Since all these processes can affect the CRE spectrum after its injection by the sources, the observed spectrum is sensitive to the environment, i.e., to where and how electrons (and positrons) originate and propagate through the Galaxy.

Recent results from the ATIC [7], PPB-BETS [8], HESS [9, 10], PAMELA [11], and Fermi LAT [2] collaborations have shed new light on the origin of CREs. The ATIC and PPB-BETS teams reported evidence for an excess of electrons in the range 300–700 GeV compared to the background expected from a conventional homogeneous distribution of cosmic-ray (CR) sources. The HESS team reported a spectrum that steepens above ~ 900 GeV, a result which is consistent with an absence of sources of electrons above ~ 1 TeV within 300–400 pc. The PAMELA Collaboration reports that the ratio of the positron flux to the total flux of electrons and positrons increases with energy [11], a result which has significant implications. The majority of CR positrons (and some electrons) are thought to be produced via inelastic collisions between CR nuclei and interstellar gas (e.g. [12]). For this case of secondary production, the source spectrum for the CR positrons mirrors that of the CR nuclei and is steeper than the injection spectrum of primary CREs. After propagation, the secondary CR positron spectrum remains steeper, and this should give a $e^+/(e^+ + e^-)$ ratio that falls with energy. Therefore, some additional component of CR positrons appears to be required. The Fermi result either requires a reconsideration of the source spectrum and/or the propagation model or indicates the presence of a nearby source. However, the excess of events reported by ATIC and PPB-BETS was not detected by

the LAT.

The measurements described above disagree in their details with most previous models (e.g. [6, 12, 13]) in which CREs were assumed, for the sake of simplicity, to be produced in sources homogeneously distributed throughout the Galaxy. Many recent papers have revisited the CR source modeling, exploring the possibility of nearby sources whose nature could be astrophysical (e.g. pulsars) or “exotic” (see [14] and references therein).

In this paper, we describe the procedures for event energy reconstruction, electron candidate selection, and our assessment of the instrument response functions. An important cross-check of our analysis is provided by a subset of events having longer path lengths through the calorimeter and therefore better energy resolution than the full data set. The consistency of the spectrum derived using this subset and that derived using the full data set indicates that the energy resolution assumed in our previously published work [2] for events ≥ 50 GeV is indeed adequate. Finally we discuss the inferred spectrum of CR electrons and its possible interpretation.

Section II describes various aspects of our analysis method. Section III contains a thorough discussion of our efforts to minimize and characterize the systematic uncertainties in the analysis. The results are presented and discussed in Section IV.

II. ANALYSIS APPROACH

A. Overview

The LAT is a pair-conversion gamma-ray telescope designed to measure gamma rays in the energy range from 20 MeV to greater than 300 GeV. Although the LAT was designed to detect photons, it was recognized very early that it would be a capable detector of high-energy electrons [15, 16]. The LAT is composed of a 4×4 array of identical towers that measure the arrival direction and energy of each photon. Each tower is comprised of a tracker and a calorimeter module. A tracker module has 18 x - y planes of silicon-strip detectors, interleaved with tungsten converter foils, with a total of 1.5 radiation lengths (X_0) of material for normally-incident particles. In order to limit the power consumption and reduce the data volume, the tracker information at the single-strip level is digital (i.e., the pulse height is not recorded). However, some information about the charge deposition in the silicon detectors is provided by the measurement of the time over threshold (TOT) of the trigger signal from each of the tracker planes; see [17] for further details on the architecture of the tracker electronics system. A calorimeter module with $8.6 X_0$ for normal incidence, has 96 CsI(Tl) crystals, hodoscopically arranged in 8 layers, aligned alternately along the x and y axes of the instrument. A segmented anticoincidence detector (ACD), which tags $> 99.97\%$ of the charged particles, covers the tracker module array. The electronic subsystem includes a robust programmable hardware trigger

and software filters. The description of the detector calibrations that are not covered in this paper can be found in [18].

The CRE analysis is based on the gamma-ray analysis, as described in [1]. The main challenge of the analysis is to identify and separate 7–1000 GeV electrons from all other species, mainly CR protons. The analysis involves a trade-off between the efficiency for detecting electrons and that for rejecting interacting hadrons. The high flux of CR protons and helium [19, 20] compared to that of CREs dictates that the hadron rejection must be 10^3 – 10^4 , increasing with energy.

The development of the LAT included careful and accurate Monte Carlo (MC) modeling. The details of the MC simulations are described in Sec. II B. To validate the responses of the instrument, we built and modeled a beam test unit using spare flight towers. This unit was subjected to comprehensive calibration data taking using beams of photons, electrons, protons and nuclei. Beam-test data were compared to the results of the MC modeling, and the detector response was modified in the MC code, as discussed in Sec. II C. In Sec. II D we discuss the cuts that select the final data sample.

B. Monte Carlo simulations

Monte Carlo simulations played an essential role in the design of the LAT and optimization of the data analysis. These simulations have been used to develop the electron selection algorithms to remove interacting hadron background, and to determine the instrument response functions including efficiency, effective area, and solid angle for spectral reconstruction.

We generate input distributions of gamma rays and charged particles with fully configurable spatial, temporal, and spectral properties, which allow us to simulate CR particles, beam-test data, ground calibration data, and even a complete gamma-ray sky. The simulated events are fed into a detailed model of the instrument with all its materials down to individual screws as well as a simplified model of the Fermi spacecraft and material below the LAT. The model of the instrument and the physical interaction processes are based on the GEANT4 package [21], widely used in high-energy physics. The details of the MC simulations for the electron analysis are given in [22]. The MC simulations produce both raw and processed data, include the effects of statistical processes such as Landau fluctuations in energy loss, and simulate the on-board processing and trigger algorithms. Output from the simulation is fed into the same reconstruction chain as data, thus producing the output quantities that can be compared with data from flight, calibration runs, beam tests, etc.

In the present analysis we have used three types of simulations: electrons only, full CR and Earth albedo particle populations, and protons only. For simulating CREs, other CR particles, and Earth albedo particles, a model of

the energetic particle populations in the Fermi orbit has been developed [1]. The modeled fluxes of the particles were constructed using the results from CR experiments, when available. Where data were missing (e.g., the angular distribution of albedo protons below the geomagnetic cutoff from Galactic cosmic rays interacting with the atmosphere), published simulations were used (e.g. see [23]). The model includes all the components of charged Galactic cosmic rays (protons, antiprotons, electrons, positrons, and nuclei up through iron) from the lowest geomagnetic cutoff rigidity seen by the spacecraft up to 10 TeV, together with reentrant and splash Earth albedo particles (neutrons, gamma rays, positrons, electrons, and protons) within the energy range 10 MeV to 20 GeV (their rates become negligible at higher energy). The fluxes are taken to be the same as those observed near solar minimum (i.e., maximum Galactic cosmic-ray intensities), the condition that applied for the data-taking period covered in this paper.

To study the effective acceptance for electrons and also to characterize the residual background from hadrons, we needed a large sample of simulated events. Our total Monte Carlo simulations for the present analysis used approximately 400 CPUs for 80 days, corresponding to ~ 90 CPU years computing time, and was the most resource-intensive part of the analysis. To enhance the number of simulated events at high energies, we often use input power-law spectra with equal numbers of counts per decade ($dN/dE \propto E^{-1}$). The results then easily can be weighted to be valid for the spectral index of interest.

C. Beam test validation

The analysis described in this paper relies strongly on MC simulations for development of the event selection, performance parameterization, and estimation of residual background. In order to validate the simulations, a beam-test campaign was performed in 2006 on a calibration unit (CU) built with flight spare modules integrated into a detector consisting of two complete tracker plus calorimeter towers, an additional third calorimeter module, several anticoincidence tiles, and flightlike readout electronics. The CU was exposed to a variety of beams of photons (up to 2.5 GeV), electrons (1–300 GeV), hadrons (π and p , a few GeV–100 GeV), and ions (C, Xe, 1.5 GeV/n) over 300 different instrumental configurations at the CERN and the GSI Helmholtz Centre for Heavy Ion Research accelerator complexes [24]. Such a large data sample allows a direct comparison with simulations over a large portion of the LAT operational phase space.

Validations studies were conducted by systematically comparing data taken in each experimental configuration to a simulation corresponding to that configuration. Distributions of the basic quantities used for event reconstruction and background rejection analysis, such as tracker clusters, calorimeter, and anticoincidence detector energy deposits and their spatial distributions, were compared.

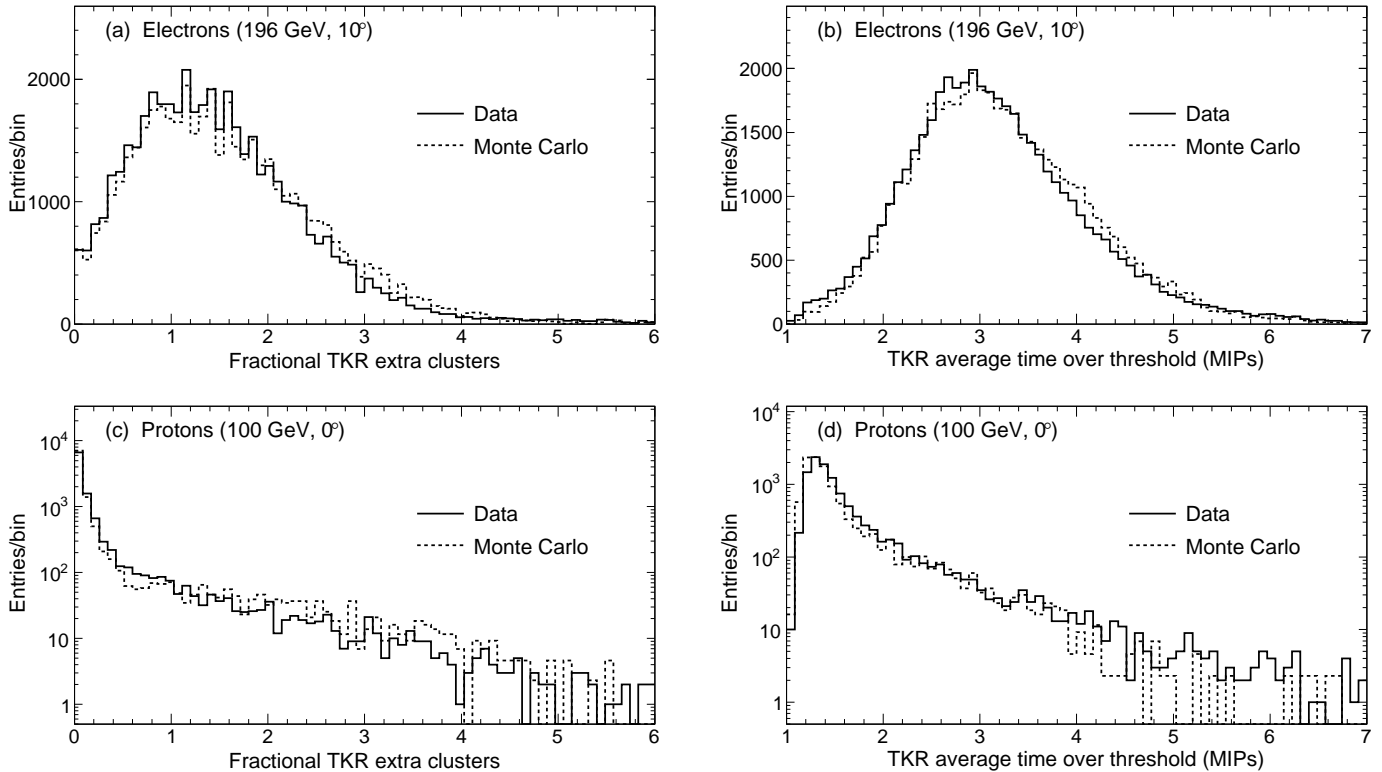


FIG. 1: Comparison of beam-test data (solid line) and MC simulations (dashed line) for two fundamental tracker variables used in the electron selection: the number of clusters in a cone of 10 mm radius around the main track (left panels) and the average time over threshold (right panels). Both variables are shown for an electron and a proton beam.

Differences were minimized after modifying the Monte Carlo simulation, based on the GEANT4 toolkit [21], to best match the data. The main changes were to improve the description of the geometry and the materials in the instrument and along the beam lines, and the models describing electromagnetic (EM) and hadronic interactions in the detector. Data were corrected for environmental effects that were found to affect the instrumental response, such as temperature drifts and beam-particle rates.

We found that EM processes are well described by the standard LHEP libraries [21], the only exception being the *Landau-Pomeranchuk-Migdal* effect (LPM, [25]), which was found to be inaccurately implemented. Based on our findings, this was fixed in the GEANT4 release itself¹. The erroneous implementation produced a significant effect in the description of EM cascades at energies as low as ~ 20 GeV. The LAT is in fact sensitive to the onset of the LPM effect, as it finely samples the longitudinal and lateral shower development.

Tuning the GEANT4 simulation of hadronic interactions to the actual instrumental response requires choos-

ing among the many alternative cross-section algorithms and interaction models that are specific to the energy range of interest. GEANT4 offers such flexibility through a choice of different implementations from a list of possibilities [21]. We found that the simulations that best reproduce the hadronic interactions recorded in the CU are obtained when using the Bertini libraries at low energies (< 20 GeV) and the QGSP code at higher energies (> 20 GeV) [26, 27]. With such models, the agreement between data and Monte Carlo simulations for hadronic cascades is not perfect, but appears to be sufficient to safely estimate the residual hadronic contamination.

These codes were incorporated in both the CU and LAT simulations. The average values of the distributions of all basic subsystem variables are typically reproduced by the simulations to within $\pm 5\%$ for EM interactions and $\pm 10\%$ for hadronic interactions (with maximal discrepancies twice as large at the limit of instrument acceptance and for the highest energies). However, essential variables such as the transverse size of showers in the calorimeter, the distribution of extra clusters in the tracker, and the average time over threshold along the best track (see, for example, Fig. 1) are well reproduced. Residual differences between the beam test data and the simulations are all included in the systematic errors evaluated according to the prescription in Sec. III D.

Beam-test electron data were also used to validate our

¹ The LAT CU data were used as a benchmark for the GEANT4 EM physics classes including the LPM effect; GEANT4 releases 9.2-beta-01 and later contain the correct implementation.

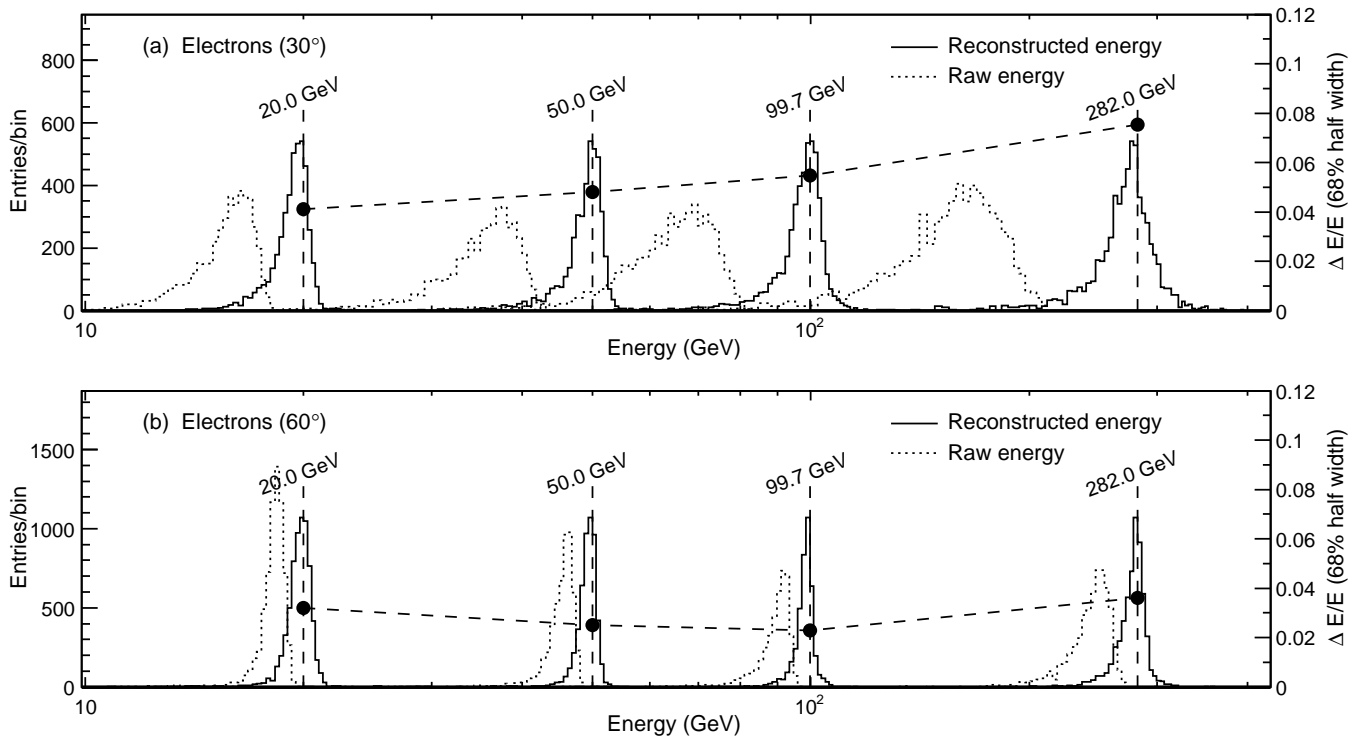


FIG. 2: Plots of the measured raw energy and reconstructed energy for different beam energies at 30° (top panel) and 60° (bottom panel). The points connected by the dashed line represent, for each configuration, the energy resolution (half-width of the 68% event containment; see Sec. II E for details), which can be read on the right axis. The vertical dashed line represents, for each case, the nominal beam energy. It is clear that the leakage correction is much more pronounced at relatively smaller angles

evaluation of the energy resolution. As explained in Sec. II E, high-energy EM showers are not fully contained in the LAT CU, and an evaluation of the shower fraction leaking from the CAL is needed to correctly reconstruct the shower energy. The effect of the leakage correction in the energy reconstruction algorithm can be seen directly in Fig. 2, where the raw energy deposit and the reconstructed energy distributions are shown for several electron beams impacting the CU. The energy resolution derived from the peak widths is plotted on the right axis. The agreement between data and our simulations is shown in Fig. 3.

After improving the simulation as described above, an important residual discrepancy between the simulation and the beam test data was found in the raw energy deposited in the CU, which was measured to be 9% higher, on average, than predicted, with an asymmetric spread ranging from -6% to $+1\%$, slightly depending on the energy and incident angle. This difference was corrected in beam test data using a simple scaling factor on the CU energy measurement, thus providing a good agreement between the energy deposit along the shower axis with the Monte Carlo simulations, as can be seen in Fig. 4.

The origin of this 9% scaling factor is unknown. It may have to do with an imperfect calibration of the CU calorimeter modules or residual effects from temperature and rates at the beam test that were not accounted for in the data analysis. Further studies are now in progress

with flight data. For this reason the LAT data are not corrected with this scaling factor, but we include a systematic uncertainty in the LAT energy scale of $+5\%$ to -10% .

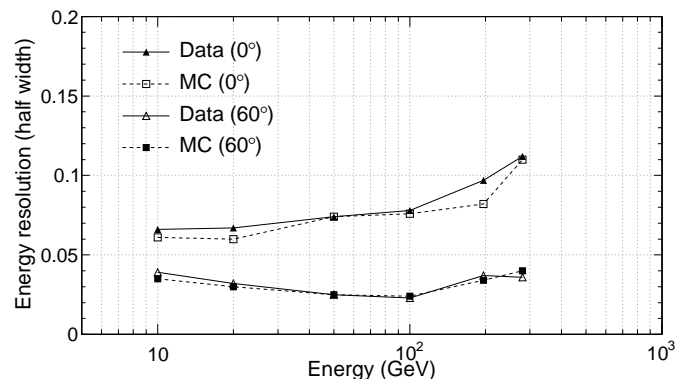


FIG. 3: Comparison of beam-test data (triangles) and Monte Carlo simulations (squares) for the energy resolution for electron beams entering the CU at 0° and 60° and energies from 10 to 282 GeV. Lines connecting points are to guide an eye.

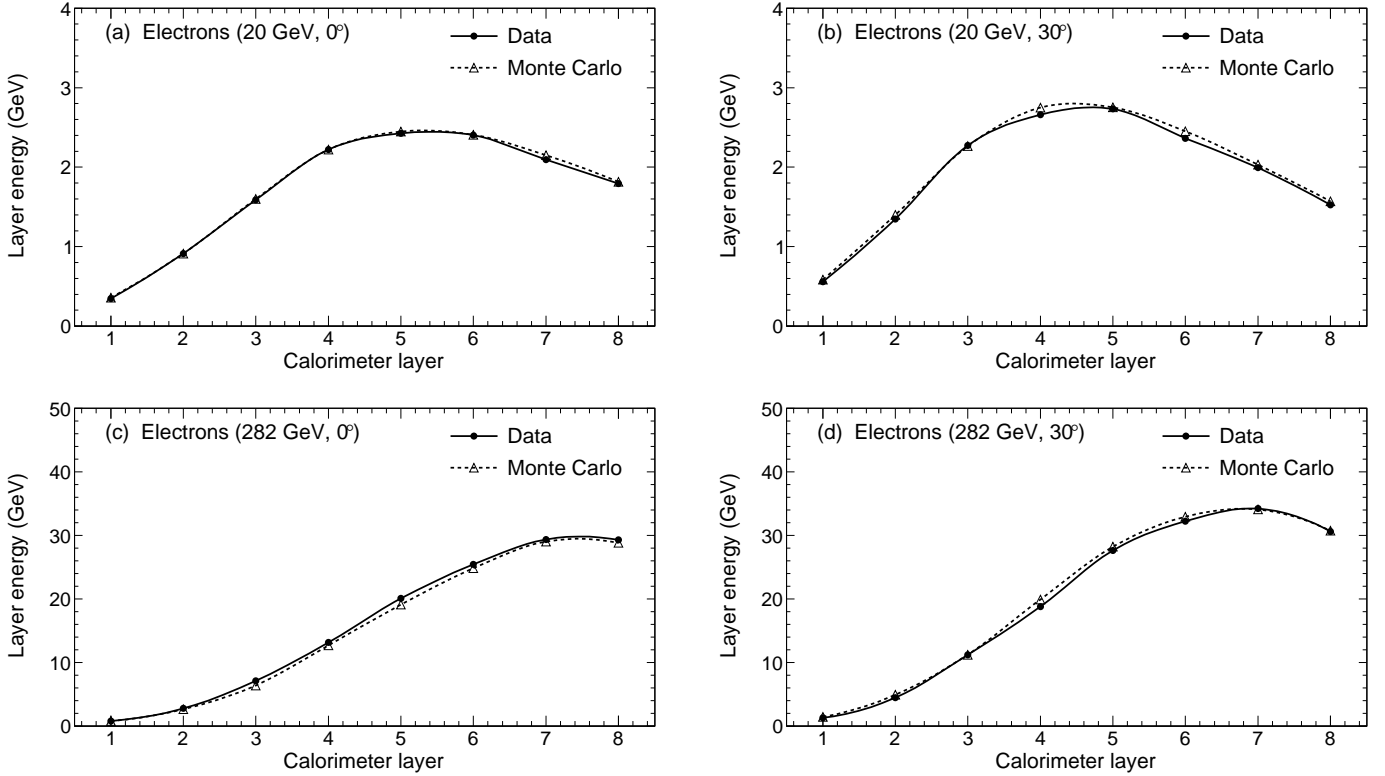


FIG. 4: Comparison of beam-test data and Monte Carlo simulations for the longitudinal shower profiles for electron beams entering the CU at 0° and 30° and energies of 20 and 282 GeV.

D. Event selection

The event selection relies on the capabilities of the tracker, calorimeter, and anticoincidence subsystems, alone and in combination to discriminate between electromagnetic and hadronic event topologies. The analysis of EM showers produced in the instrument by CRE and gamma rays is very similar. For event reconstruction (track identification, energy and direction measurement, ACD analysis) and calculation of variables used in event classification we use the same reconstruction algorithms. Although based on the same techniques, the selections are of course different and specific to the electron analysis. For example, the ACD effectively separates charged particles from photons. It also provides information on the topologies of the event useful for separating electrons from protons. The electron analysis covers the energy range from a few GeV to 1 TeV while the photon analysis is currently optimized for the 100 MeV–300 GeV range.

Although some fraction of hadrons can have interactions that mimic electromagnetic events, their true energies cannot be evaluated event by event and are underestimated by our reconstruction algorithms. Generally, the shapes of hadronic showers differ significantly from EM showers. The most powerful separators are the comparative lateral distributions. Electromagnetic cascades are tightly confined, while hadronic cascades that leave comparable en-

ergy in the calorimeter tend to deposit energy over a much wider lateral region affecting all three detector subsystems. The nuclear fragments tend to leave energy far from the main trajectory of the particle. Thus hadron showers have larger transverse sizes in the calorimeter, larger numbers of stray tracks in the tracker, and larger energy deposits in more ACD tiles.

Since the phenomenology of the EM cascades and hadron interactions varies dramatically over the energy range of interest, we developed two independent event selections, one tuned for energies between 20 and 1000 GeV and the other for energies between 0.1 and 100 GeV, which we shall refer to as HE and LE. The HE analysis takes advantage of the fact that the on-board filtering (event selections designed to fit the data volume into the available telemetry bandwidth with a minimal impact on the photon yield) is disengaged for events depositing more than 20 GeV in the calorimeter. The source of data for the LE selection is an unbiased sample of all trigger types, prescaled on-board so that one out of 250 triggered events is recorded without filtering. The region of overlap in energy, between 20 and 80 GeV, allows us to cross-check the two independent analyses. Above about 80 GeV the number of events in the prescaled sample becomes too low to be useful.

The event selection process must balance removal of background events and retaining signal events, while lim-

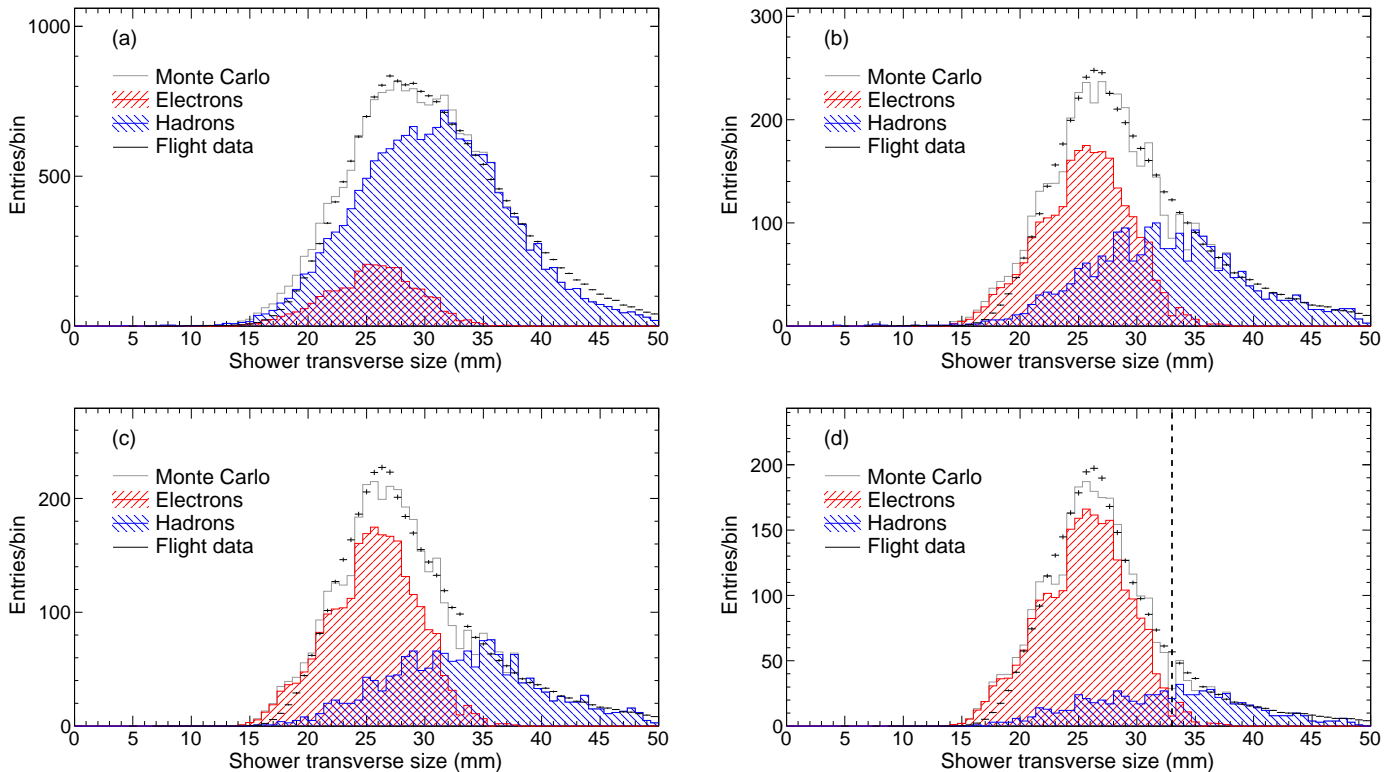


FIG. 5: (color online). Distribution of the shower transverse size in the calorimeter for the energy interval 133–210 GeV at different stages of the HE selection: (a) after the cuts on the calorimeter variables except the one on the transverse size itself, (b) adding the selection on the tracker, (c) on the ACD and (d) on the probability that each event is an electron based on a classification tree analysis. The vertical dashed line in panel (d) represents the value of the cut on this variable. The Monte Carlo distribution (gray line) is the sum of both the electron and hadron components. The simulations have poorer statistics (as reflected in larger bin-to-bin fluctuations) and are scaled to the flight data.

iting systematic uncertainties. We first reject those events that are badly reconstructed or are otherwise unusable. We require at least one reconstructed track and a minimum energy deposition (5 MeV for LE and 1 GeV for HE) and, for HE events, a pathlength longer than $7 X_0$ in the calorimeter. We keep only events with zenith angle $< 105^\circ$ to reduce the contribution from Earth albedo particles.

The next step is to select electron candidates based on the detailed event patterns in the calorimeter, the tracker, and the ACD subsystems.

The calorimeter plays a central role by imaging the shower and determining its trajectory. We fit both the longitudinal (for determining energy) and transverse shower distributions and compare them to the distributions expected for electromagnetic cascades. Figure 5 shows the sequence of four successive cuts on the data in a single energy bin, for the transverse shower size in the calorimeter. This figure illustrates the difference in transverse shower size between electrons and hadrons, and illustrates how all three LAT subsystems contribute to reduce the hadron contamination.

The tracker images the initial part of the shower. As shown earlier in Fig. 1, electrons are selected by having larger energy deposition along the track and more clus-

ters in the vicinity (within ~ 1 cm) of the best track, but which do not belong to the track itself. As illustrated in Figs. 1(a) and 1(c), the fraction of these extra clusters is, on average, much higher for energetic electrons than for protons. The average energy deposition in the silicon planes (which we measure by means of the time over threshold) is also higher for electrons, as can be seen in Fig. 1(b) and 1(d).

The ACD provides part of the necessary discrimination power. Photons are efficiently rejected using the ACD in conjunction with the reconstructed tracks. A signal in an ACD tile aligned with the selected track indicates that the particle crossing the LAT is charged. Hadrons are removed by looking for energy deposition in all the ACD tiles, mainly produced by particles backscattering from the calorimeter. Two examples of this effect can be seen in Fig. 6. Figure 6(a) shows the total energy deposition in the ACD tiles for the LE analysis; the hadrons are more likely to populate the high-energy tail. Figure 6(b) shows the average energy per tile in the HE analysis; it is significantly higher for hadrons than for electrons, due to backscplash from nuclear cascades.

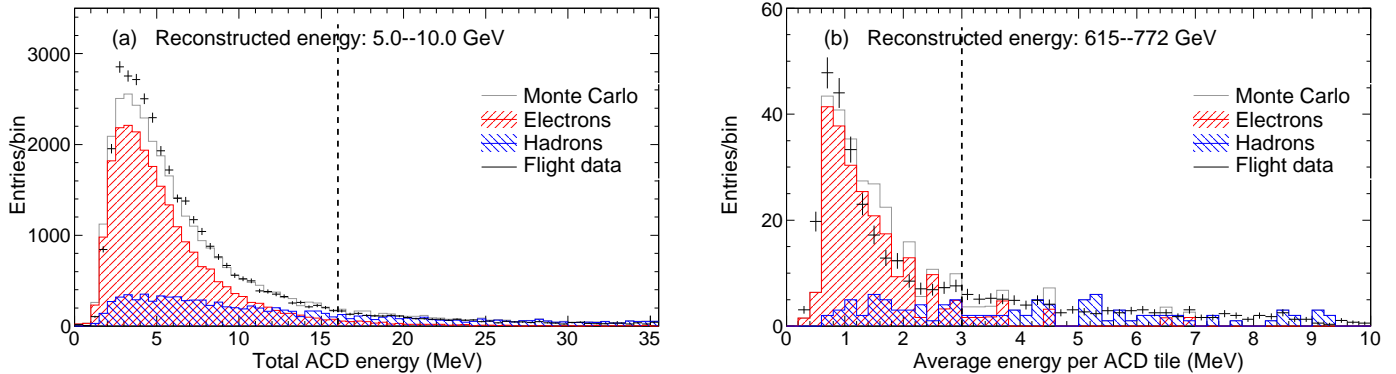


FIG. 6: (color online). Distribution of (a) total energy deposition in the ACD used in LE selection and (b) average energy per ACD tile used in HE. The vertical dashed line corresponds to the cut value on the variables in question. Both distributions are shown after the cuts on all other variables have been applied.

A classification tree (CT) analysis² provides the remaining hadron rejection power necessary for the CRE spectrum measurement.

We identified the quantities (variables) derived from the event reconstructions that are most sensitive to the differences between electromagnetic and hadronic event topologies. For example, the multiplicity of tracks and the extra hits outside of reconstructed tracks is useful for rejecting interacting hadrons. Variables mapping the shower development in the calorimeter are also important. The CTs are trained using simulated events and, for each event, predict the probability that the event is an electron. The cut that we have adopted on the resulting CT-predicted electron probability is energy dependent. For HE analysis, a higher probability is required as energy increases. These cuts give us a set of candidate electron events with a residual contamination of hadrons that cannot be removed on an event-by-event basis. The remaining contamination must be estimated using the simulations and will be discussed in Sec. III B.

Though the simulations are the starting point for the event selection, we systematically compare them with the flight data as illustrated in Figs. 5–7. The input energy spectra for all the particles are those included in the model of energetic particles in the Fermi orbit (Sec. II B), with the exception of the electrons. For the electrons we use instead a power-law spectrum that fits our previous publication [2]. For any single variable we use the signal and proton background distributions at the very end of the selection chain (after the cuts on all the other variables have been applied) to quantify the additional rejection power provided by that particular variable. Any variables for which the data-MC agreement was not satisfactory were not used in any part of the selection.

The procedure used to characterize the discrepancies be-

tween data and Monte Carlo and quantify the associated systematic uncertainties will be described in Sec. III D. We stress, however, that there is a good qualitative agreement (both in terms of the shapes of the distributions and in terms of the relative weights of the electron and hadron populations) in all the energy bins and at all the stages of the selection. This is a good indication of the self-consistency of the analysis and that both the CR flux model and detector simulation adequately reproduce the data.

E. Energy reconstruction

As mentioned in the previous section, the electron energy reconstruction is performed using the algorithms developed for the photon analysis [1]. These algorithms are based on comprehensive simulations and validated with the beam test data [24].

The total depth of the LAT, including both the tracker and the calorimeter, is $10.1 X_0$ on axis. The average amount of material traversed by the candidate electrons, integrated over the instrument field of view, is $12.5 X_0$. However, for electromagnetic cascades $\gtrsim 100$ GeV a significant fraction of the energy is not contained in the calorimeter. Here, the calorimeter shower imaging capability is crucial in order to correct for the energy leakage from the sides and the back of the calorimeter and through the gaps between calorimeter modules.

The event reconstruction is an iterative process [1]. The best track provides the reference axis for the analysis of the shower in the calorimeter. The energy reconstruction is completed only after the particle tracks are identified and fitted. Following this procedure, each single event is fed into three different energy reconstruction algorithms:

- a) a parametric correction method based on the energy centroid depth along the shower axis in the calorimeter in combination with the total energy absorbed — valid over the entire energy range for the LAT;

² The reader can refer to [28] for a comprehensive review of the use of data mining and machine learning techniques in astrophysics.

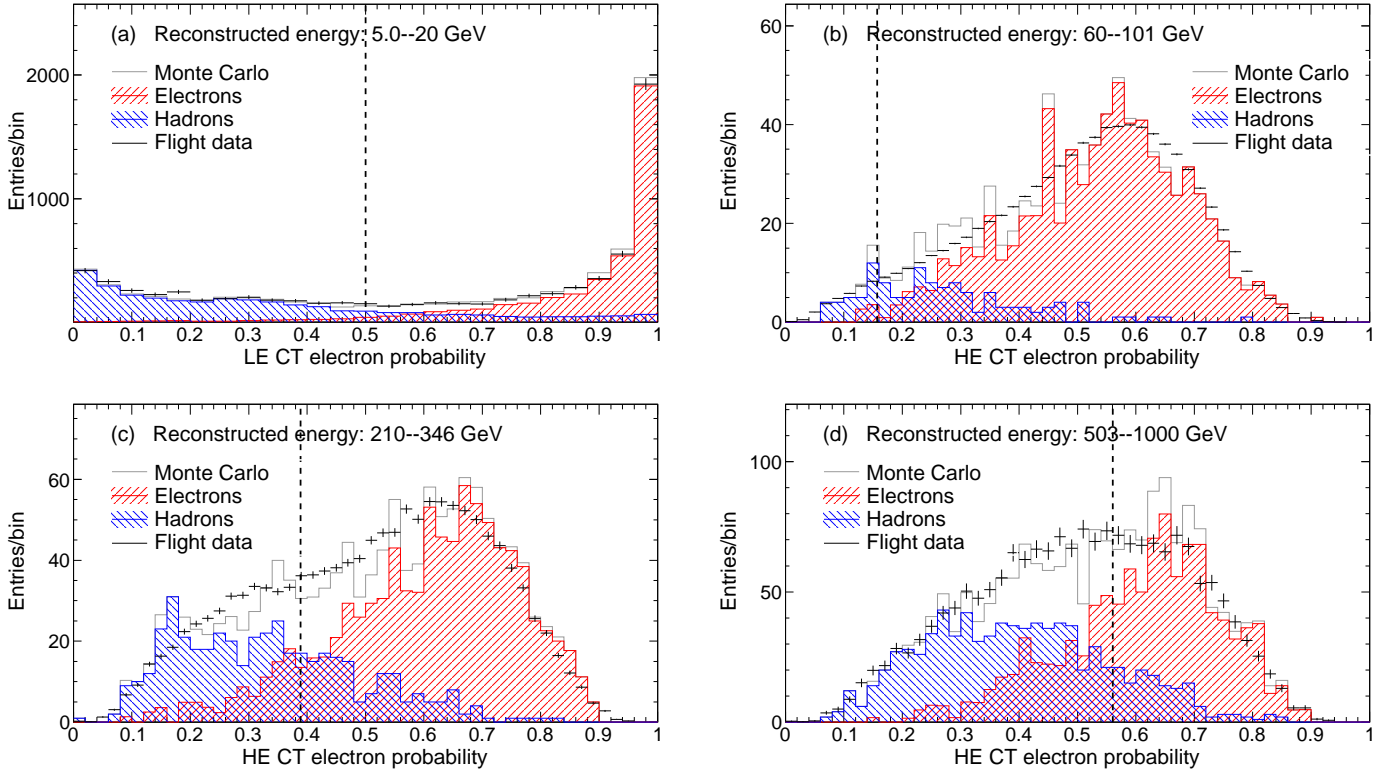


FIG. 7: (color online). Distribution of CT-predicted probability (a) for LE analysis and (b), (c), and (d) for HE analysis in different energy intervals. Monte Carlo generated distributions are compared with flight distributions. The cut value is a continuous function of energy and is represented by the vertical dashed line in each panel. The distributions are shown after the cuts on all other variables have been applied.

- b) a maximum likelihood fit, based on the correlation between the total deposited energy, the energy deposited in the last layer of the calorimeter and the number of tracker hits — valid up to 300 GeV; and
- c) a three-dimensional fit to the shower profile, taking into account the longitudinal and transverse development — valid above 1 GeV.

For each event the best energy reconstruction method is then selected by means of a CT analysis similar to that described in Sec. IID. The classifier is trained on a Monte Carlo data sample and exploits all the available topological information to infer which energy estimate is closest to the true energy for the particular event being processed. The final stage of the energy analysis, again based on a set of CTs, provides an estimate of the quality of the energy reconstruction, which we explicitly use in the analysis to reject events with poorly measured energy.

At high energies (and especially above 300 GeV, where the likelihood fit is no longer available), the three-dimensional fit to the shower profile is the reconstruction method chosen for the vast majority of events. This method takes into account the saturation of the calorimeter readout electronics that occurs at ~ 70 GeV for an individual crystal. However above ~ 1 TeV the number of saturated crystals increases quickly, requiring a more

complex correction. This is beyond the scope of the current paper and will be addressed in subsequent publications. We therefore limit ourselves to events with energies < 1 TeV.

The performance of the energy reconstruction algorithm has been characterized across the whole energy range of interest using Monte Carlo simulations of an isotropic $1/E$ electron flux. We divided the energy range into 6 partially overlapping bins per decade and quantified the bias and the resolution in each bin, based on the resulting energy dispersion distributions (defined as the ratio between the reconstructed energy and the true energy, as shown in Fig. 8).

The energy dispersion distribution in each energy window is fitted with a log-normal function and the bias is calculated as the deviation of the most probable value of the fit function from 1. This bias is smaller than 1% over the entire phase space explored. We characterize the energy resolution by quoting the half-width of the smallest window containing 68% and 95% of the events in the energy dispersion distributions. Those windows are graphically indicated in Fig. 8 and correspond to 1 and 2 sigma, respectively, in the ideal case of a Gaussian response. The energy resolution corresponding to a 68% half-width containment is about 6% at 7 GeV and increases as the energy increases, reaching 15% at 1 TeV as shown in Fig. 9. The

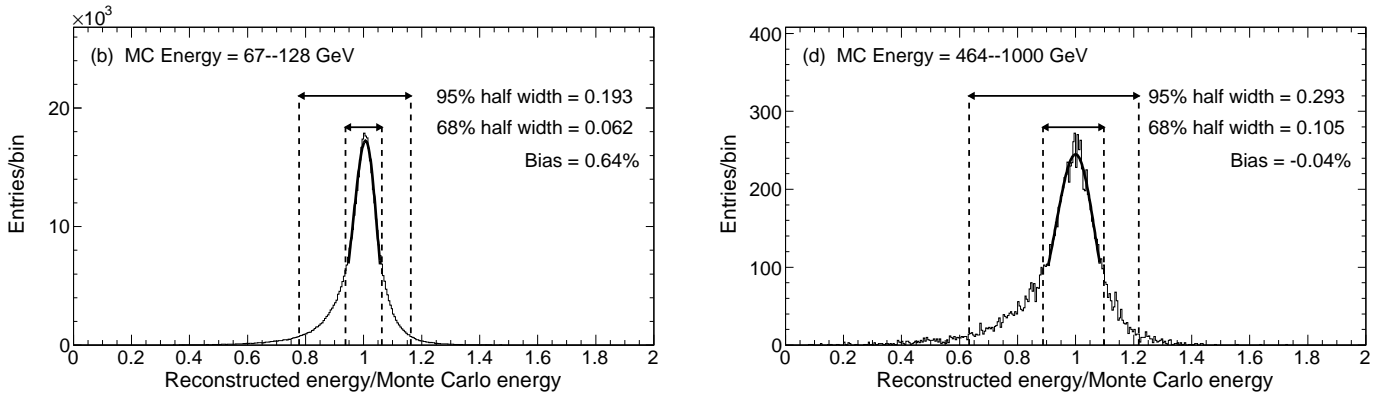


FIG. 8: Energy dispersion distributions (after the HE selection cuts have been applied) in two sample bins. The 68% and the 95% containment windows, defining the energy resolution, are represented by the horizontal double arrows. The fractional bias is defined as the deviation from unity of the position of the most probable value of the log-normal function used for fitting.

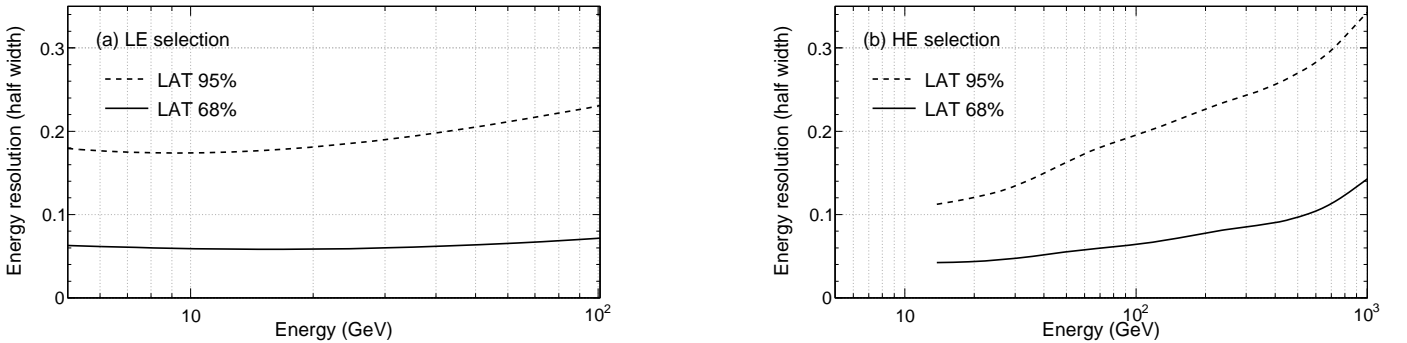


FIG. 9: Energy resolution (half-width of the 68% and 95% energy dispersion containment windows) for the LE (left panel) and the HE (right panel) analysis.

95% containment is useful to quantify the tails of the distribution and is within a factor 3 of the 68% containment. The deviation with respect to a Gaussian distribution is mainly due to a higher probability to underestimate the energy than to overestimate it and is reflected in the low-energy tails in Fig. 8. We verified, with our simulations, that the energy response does not generate any discontinuity that could create spurious features in the spectrum.

III. SPECTRAL ANALYSIS

A. Instrument acceptance

The instrument acceptance for electrons, or effective geometric factor (EGF), is defined as a product of the instrument field of view and its effective area. To calculate the EGF we use a Monte Carlo simulation of an isotropic electron spectrum with a power-law index of $\Gamma = 1$ (the same simulation described in Sec. IIE). In this case,

$$\text{EGF}_i = A \times \frac{N_i^{\text{pass}}}{N_i^{\text{gen}}} \quad (1)$$

where N_i^{gen} and N_i^{pass} are, respectively, the number of generated events and the number of events surviving the selection cuts in the i^{th} energy bin. The normalization constant A depends on the area and the solid angle over which the events have been generated.

The EGF for LE and HE events is shown in Fig. 10. The HE EGF has a peak value of $\sim 2.8 \text{ m}^2\text{sr}$ at an energy $E \sim 50 \text{ GeV}$. The falloff below 50 GeV is due to the on-board filtering (see Sec. IID), while the decrease for energies above 50 GeV is due to the energy dependence of the event selection. The LE EGF in Fig. 10 has been multiplied by a factor of 250 for graphical clarity. For energies below 30 GeV its value is almost constant while for higher energies it decreases rapidly. This effect is due to the fact that the LE event selection is optimized for relatively low energies. The statistical error on the EGF is less than $\sim 1\%$ for each energy bin of the reconstructed spectrum for both LE and HE.

B. Correction for residual contamination

We estimate the contamination in each energy bin by applying the selection cuts to the on-orbit simulation to

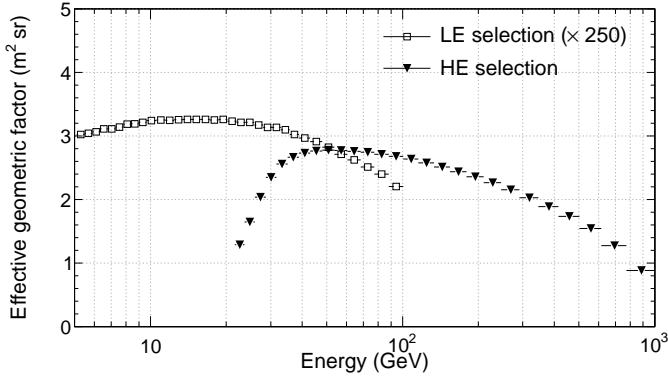


FIG. 10: Effective geometric factor for LE (squares, multiplied by a factor 250) and HE events (triangles)

determine the rate of remaining background events (protons and heavy nuclei). To correct for the contamination, this rate is subtracted from that of the flight electron candidates (shown in Fig. 11 for the HE analysis). With this procedure the contribution to the systematic uncertainty due to the residual contamination depends on the energy spectra for hadrons in our simulation and not on the one for electrons (see Sec. IIID). The contamination (defined as the ratio between simulated residual hadron rate and total event rate) ranges from $\sim 4\%$ at 20 GeV to $\sim 20\%$ at 1 TeV for the HE selection while for LE is $\sim 10\%$ at 7 GeV increasing with energy up to $\sim 18\%$ at 80 GeV. Note that the LE analysis (which is independent of the HE analysis) deals with large variation in the event topology, especially at its low-energy end; also it was optimized for the efficiency for electrons to compensate for lower input statistics. It is reflected in slightly higher (but still under 20%) residual hadron contamination.

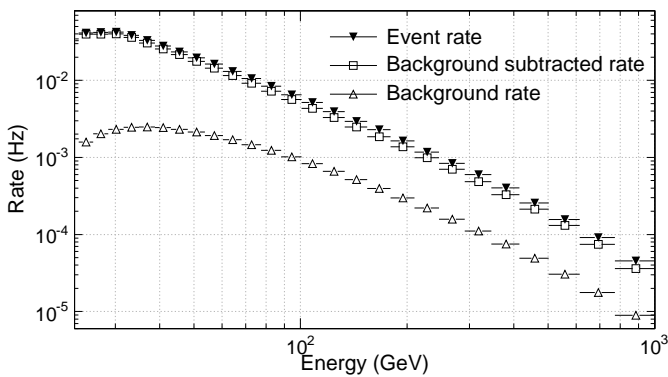


FIG. 11: Flight rate of electron candidates after HE selection (inverted triangles), corresponding simulated rate of hadron events (open triangles) and resulting rate of electrons (open squares) after background subtraction.

The number of simulated events generated was chosen to keep statistical fluctuation on the background rate small

compared to the systematic uncertainties.

As a cross-check, we also carried out Monte Carlo simulations using only protons with spectral index $\Gamma = 1$, thereby enriching the sample statistics with high-energy events. After applying the HE selection cuts, we determine the rate of residual proton events corresponding to a spectral index of 1, and reweight it to derive the residual proton event rate corresponding to the real CR proton spectral index of 2.76. We add 5% to this rate in order to take into account the contribution of heavy nuclei, mainly helium, which was not simulated. The resulting rate agrees within statistical errors with that obtained using the on-orbit flux model.

As mentioned in Sec. II D, the ACD is very effective in removing gamma-ray initiated events. To check the gamma-ray contamination in our electron candidate sample, we use the all-sky average gamma-ray flux measured by the LAT and extrapolate it over the energy range of interest. We then convolve it with the effective geometric factor for gamma rays after electron selection cuts to obtain the rate of remaining gamma-ray events. The ratio of this rate to the measured event rate provides an estimate of the gamma contamination, which remains below 0.1% over the whole energy range.

C. Spectral reconstruction

Once we have the rate of electrons, the spectrum is found by dividing the event rate by the EGF (described in Sec. III A) and the width of the energy interval. The energy dispersion (which causes events to migrate to adjacent bins) is taken into account by unfolding the background-subtracted rate with a technique based on Bayes' theorem [29]. The event migration is calculated using a matrix based on the energy dispersion obtained from simulations. We found that this correction is less than 5% in all the energy intervals.

The reconstruction procedure is similar for both the LE and the HE analyses. The former is more complicated due to the presence of the Earth's magnetic field. In fact, for energies below ~ 20 GeV we need to consider the shielding effect of the geomagnetic field as characterized by the cutoff rigidity. The lowest allowed primary-electron energy is strongly dependent on geomagnetic position and decreases with increasing geomagnetic latitude. For the orbit of Fermi, the cutoff ranges between about 6 and 15 GeV.

As recognized in [30], the McIlwain L^3 parameter is particularly convenient for characterizing cutoff rigidities and has been used for selecting data in the LE analysis. Figure 12 illustrates the distribution of the McIlwain L

³ The McIlwain L parameter is a geomagnetic coordinate defined as the distance in Earth radii from the center of the Earth's tilted, off-center, equivalent dipole to the equatorial crossing of a field line.

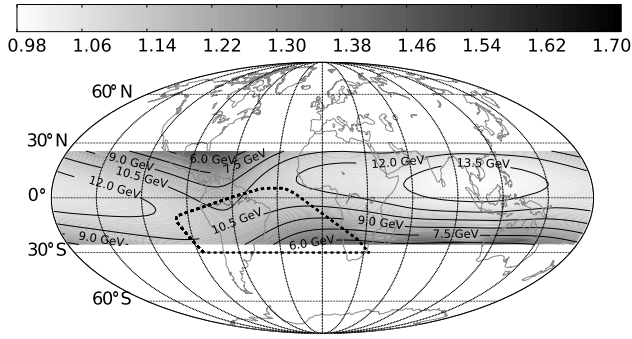


FIG. 12: Map of McIlwain L values for the Fermi orbit. Overlaid in contours are the corresponding values for vertical cutoff rigidity. These values were calculated using the 10th generation IGRF model [31], which is valid outside of the South Atlantic Anomaly (represented by the dashed black line in the figure).

parameter for the Fermi orbit. We want to stress here that the contours shown in Fig. 12 are the vertical cutoff rigidities based on the International Geomagnetic Reference Field (IGRF) model [31] and are intended for illustrative purposes only. Our analysis does not depend in any way on the vertical cutoff values from this model.

Each McIlwain L interval has an associated cutoff; we determine E_c by parameterizing the shape of the CRE spectrum as

$$\frac{dN}{dE} = c_s E^{-\Gamma_s} + \frac{c_p E^{-\Gamma_p}}{1 + (E/E_c)^{-6}} \quad (2)$$

where c_s and c_p are the normalization constants for the secondary (albedo) and primary components of the spectrum while Γ_s and Γ_p are their spectral indexes. Figure 13 illustrates how we determine E_c using Eq. 2 for three McIlwain L intervals.

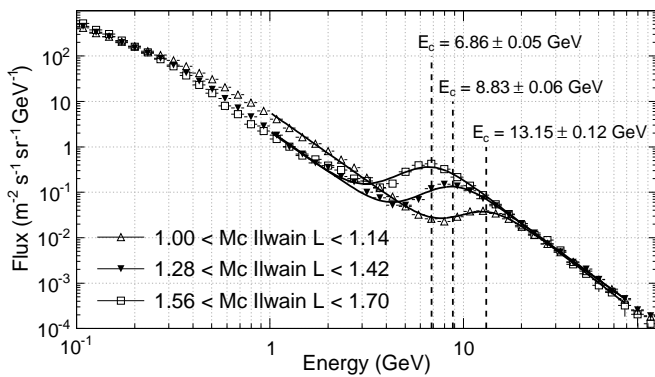


FIG. 13: The measured electron flux in three McIlwain L bins. For each bin the fit of the flux with equation 2 and the resulting estimated cutoff rigidity, E_c , is shown. As described in the text, E_c decreases for larger values of McIlwain L.

As can be seen in Fig. 13, the transition to cutoff is smoothed out due to the complexity of the particle orbits in the Earth's magnetosphere. Therefore, we increase

E_c by 15% to arrive at an effective minimum energy of the primary electron flux not affected by the Earth's magnetic field. To verify that this increase is sufficient, we have performed a series of tests to quantify the changes in the flux level as a function of this parameter and found that the final spectrum does not vary significantly for values greater than 15%. We split the LE data sample into 10 intervals of McIlwain L parameter. For each energy bin we use the interval of McIlwain L parameter whose effective minimum energy is lower than the energy in question. This procedure is illustrated in Fig. 20, where the electron spectrum is shown together with the McIlwain L intervals from which the flux was measured.

The electron flux below the geomagnetic cutoff is due to secondary electrons produced in the Earth atmosphere including reentrance albedo. Discussion of the spectrum below the cutoff is beyond the scope of this paper.

D. Assessment of systematic uncertainties

The imperfect knowledge of the EGF constitutes one of the main sources of systematic uncertainty. This is a direct consequence of the fact that the simulations we use for the evaluation of the EGF cannot perfectly reproduce the topological variables used in the electron selection. Differences between data and simulation may affect the flux measurement also through the subtraction of the hadronic background, but this contribution is relatively easier to keep under control because the contamination itself is always under 20%. In order to characterize the agreement between simulations and data, and assess the effect of the residual discrepancies, we systematically studied the variations of the measured flux induced by changes in the selection cuts around the optimal values. If the agreement were perfect the flux would not depend on the cut values. However, this is in general not true and such changes translate into systematically higher or lower flux values.

Consider a variable for which we wish to know the effect of changing cut values. We first apply all other cuts, and then vary the cut value on this variable and study the effects. The procedure we used is illustrated in Fig. 14 for one variable in one energy bin. Panel 14(a) shows how the geometric factor and the measured flux depend on the cut value. In this particular case a harsher cut translates into a systematically higher flux. This can be qualitatively understood by looking at the comparison between data and Monte Carlo simulation for the distribution of the average energy per ACD tile shown in Fig. 6(b). The distribution of this quantity in our simulation is slightly shifted toward higher energies with respect to the flight data and therefore, for any given cut, we effectively tend to underestimate the EGF (i.e., overestimate the flux). It is important to note that this variable is directly related to the topology of the backslash in the ACD, which is extremely hard to simulate, especially at very high energies.

We found that the scatter plot of the measured flux vs the geometric factor, as shown in Fig. 14(b), can be fit-

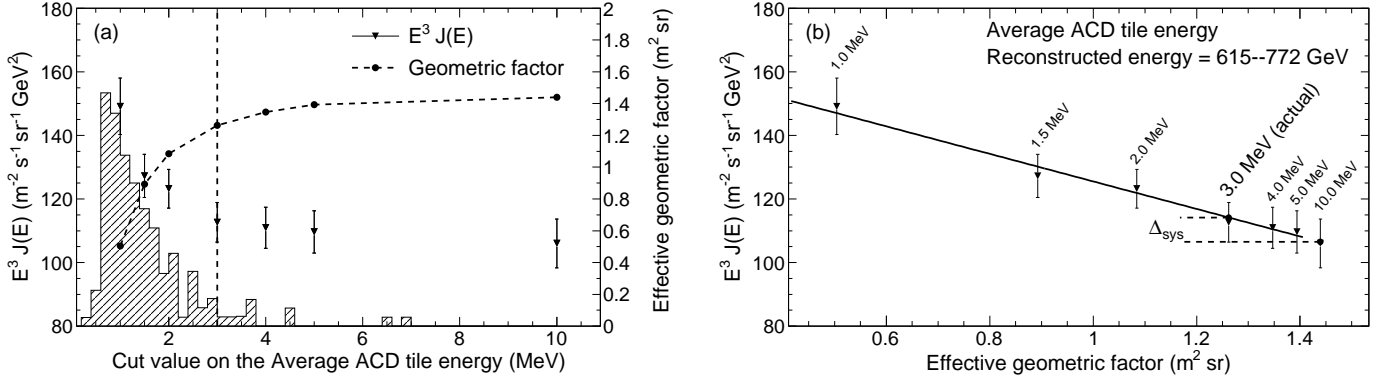


FIG. 14: Effect of cut on the average energy release per ACD tile for the energy interval 615 to 772 GeV. Panel (a) shows how the measured flux (triangles, scale on left axis) and the effective geometric factor (circles, scale on right axis) depend on the cut value. The vertical dashed line indicates the value used. For reference, the Monte Carlo distribution of the average ACD tile energy is shown. Panel (b) shows the measured flux vs the effective geometric factor for the cut values indicated.

ted reasonably well with a straight line in all the cases we encountered (the slope returned by the fit being directly related to the agreement between Monte Carlo and flight data). The fit function is used to determine the difference between the flux at the selected cut value and that measured when the cut is loose enough that the variable under study no longer contributes to the selection. We take this difference [Δ_{sys} in Fig. 14(b)] as the estimate of the systematic effect introduced by the variable itself. For the case illustrated in Fig. 14 it is 7% and represents the largest single contribution, among all the selection variables, to the total systematic error in this energy bin.

The method described here is sensitive to differential discrepancies around the cut values for both signal and background and allows us to map them to the actual measured spectrum. It has been performed separately for each energy bin and each selection variable (setting the cuts for all the other variables to the optimal values). Positive (negative) contributions, corresponding to variables for which the slope of the fit is negative (positive) are summed up in quadrature separately to provide an asymmetric bracketing of systematic uncertainty.

The error on the absolute normalization of the background flux (predominantly protons) constitutes an additional source of systematic uncertainty. We conservatively assumed a constant value of 20%, which is properly weighted with the residual contamination (Sec. III B).

The uncertainty in the absolute energy scale of the detector is also a significant contribution to the systematic error on the measurement. Assuming that this uncertainty $\Delta s/s$ is energy-independent (as the results of our beam test indicate) it translates into a rigid shift of the overall spectrum. For a given spectral index Γ the vertical component of this shift is given by $(\Gamma - 1)\Delta s/s$ (i.e., is 20% for an uncertainty of 10% on the absolute energy scale and a spectral index $\Gamma = 3$).

The simulated data sample used for the evaluation of the geometric factor and the residual contamination is large enough that any effect due to statistical fluctuations is

negligible in both the LE and the HE analysis. This is not true for the analysis with sampled statistics presented in Sec. III E.

E. Cross-check using events with long path in the instrument

In order to cross-check the impact of the energy resolution on the measured spectrum, we performed a dedicated analysis in which we selected events with the longest path lengths (at least 12 X_0) in the calorimeter. We further select events that do not cross any of the boundary gaps between calorimeter tower modules and that have sufficient track length (at least 1 X_0) in the tracker for a good direction reconstruction. For the event sample defined by these three requirements the average amount of material traversed is $\sim 16 X_0$ (see Fig. 15), ensuring that the

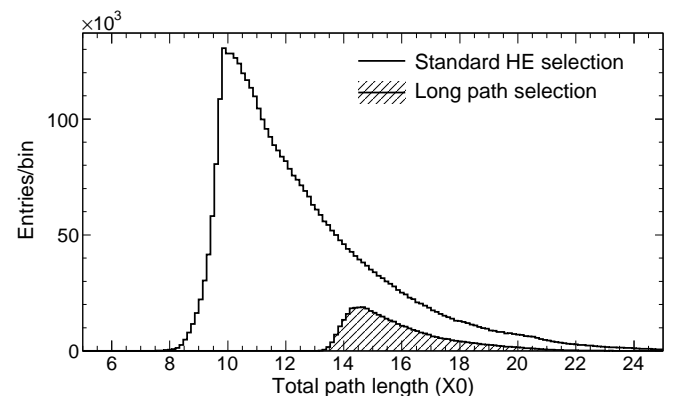


FIG. 15: Distribution of the amount of material traversed by the candidate electrons passing the long path selection, compared with that for the entire data sample used in the standard analysis (the sharp edge at $\sim 10 X_0$ in the latter reflects the total thickness of the instrument on-axis). Note the difference in the number of events.

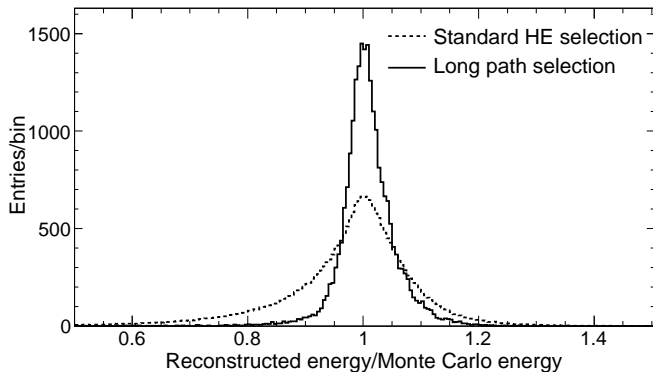


FIG. 16: Energy dispersion distribution in the energy range 242–458 GeV for the long-path selection (solid line) and the standard HE analysis (dashed line).

shower maximum is well contained in the calorimeter up to at least 1 TeV (the average depth of the shower maximum for electrons at this energy is $10.9 X_0$). Correspondingly the instrument acceptance decreases to $\sim 5\%$ of that achieved in the standard analysis described in the previous sections.

As illustrated in Figs. 16 and 17, the energy resolution for events passing this restrictive selection is significantly better than that presented in Sec. IIE for the full analysis. The energy dispersion distributions are much narrower and symmetric, with no prominent low-energy tails. The energy resolution (half-width of the 68% containment window) is around 3% at 100 GeV and increases to approximately 5% at 1 TeV.

Figure 18 shows the event rate (multiplied by E^3) for the long path length selection. There is no evidence of any significant spectral feature. The dashed line is a fit with a smooth function; the residuals of the fit are plotted in the bottom panel.

A complete assessment of the systematic uncertainties related to the discrepancies between data and simulations

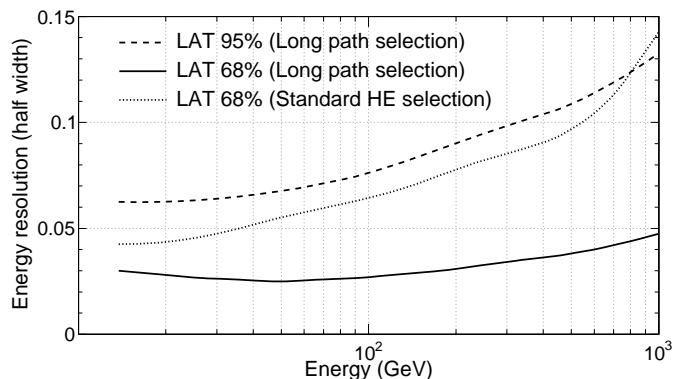


FIG. 17: Energy resolution for the long-path selection analysis. The half-width of the 68% containment window for the HE analysis, which is comparable with that of the 95% window for the more restrictive analysis, is overlaid for reference.

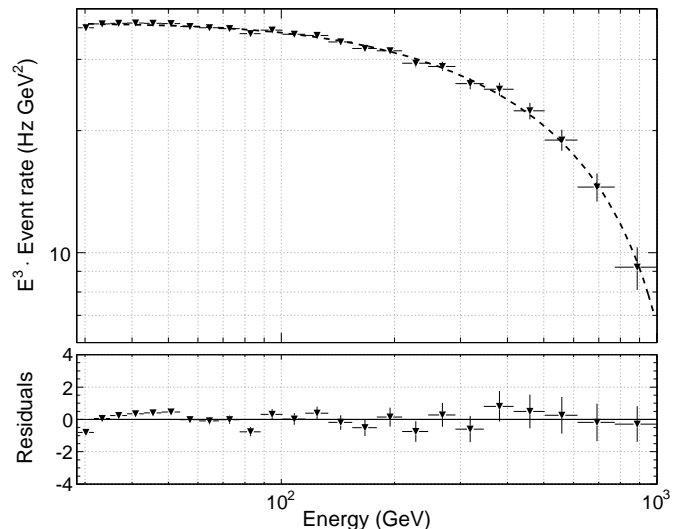


FIG. 18: Count rate multiplied by E^3 for long-path selection. The bottom panel shows residuals from the smooth function fit (dashed line in the top panel).

for this subset of data (as discussed in Sec. IIID for the full analysis) would require us, in this case, to undertake more complex simulations with about 20 times as many events; this is not possible at this time. It is reasonable to assume that such uncertainties are of the same order of magnitude as those quoted for the HE events. Because this source of systematic errors comes from the analysis of data sets of very different size, with one being only $\sim 5\%$

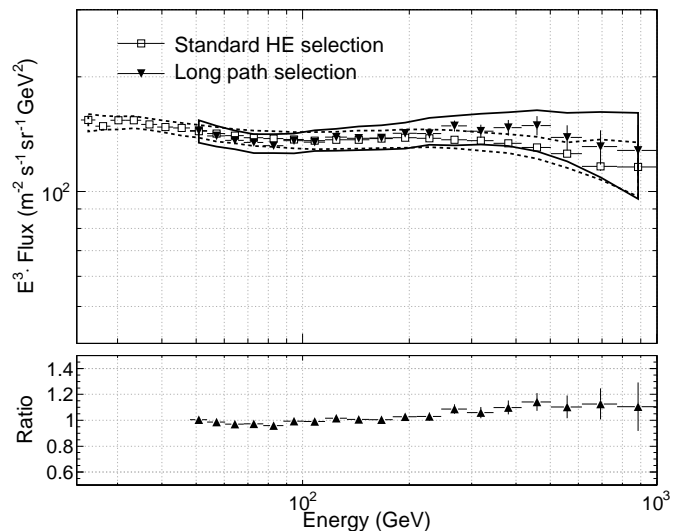


FIG. 19: Comparison of the spectra obtained with the long-path selection and the standard HE selection. The continuous lines represent the systematic uncertainties for the long-path analysis and the dashed lines for the standard analysis. The bottom panel shows the ratio of the two spectra.

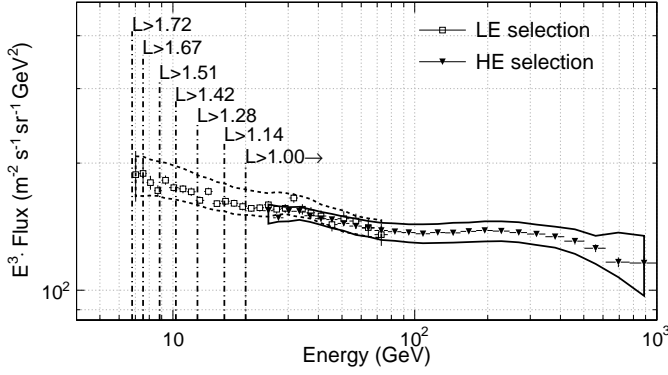


FIG. 20: Cosmic-ray electron spectra as measured by Fermi LAT for 1 yr of observations for LE events (squares) and HE events (triangles). The continuous lines represent the systematic uncertainties. The two spectra agrees within systematic errors in the overlap region between 20 GeV and 80 GeV.

of the other, we can assume that they are substantially independent.

However this assumption is not critical for our purposes, because the systematic uncertainties in the evaluation of

the EGF and the residual contamination (which again are connected to the limited size of the simulated event samples) are significantly larger, here, and in fact constitute the dominant contribution. Figure 19 shows the consistency, within the systematic errors, between the spectrum obtained with the standard analysis and that obtained with the long-path selection. This confirms that the energy resolution quoted in Sec. II E is indeed sufficient for the measurement and does not have any significant effect on the spectrum.

IV. RESULT AND DISCUSSION

We analyzed data collected in nominal sky survey mode from 4 August 2008 to 4 August 2009, for a total live time of about 265 days. The event sample after the selection is composed of 1.24×10^5 events in the LE range and 7.8×10^6 events in the HE range. For the latter analysis, the energy bins were chosen to be the full width of 68% containment of the energy dispersion, evaluated at the bin center. The resulting electron spectra are shown in Fig. 20 for the two selections. They agree within systematic errors in the overlap region between 20 GeV and 80 GeV.

TABLE I: Number of events, residual hadronic contamination, flux J_E and minimum McIlwain L value for LE analysis. Statistical error is followed by systematic error (see Sec. III D). Residual contamination is defined as the ratio between hadronic background rate and measured event rate.

Energy (GeV)	Counts	Residual contamination	J_E ($\text{GeV}^{-1} \text{s}^{-1} \text{m}^{-2} \text{sr}^{-1}$)	McIlwain L >
6.8–7.3	109	0.11	$(54.6 \pm 7.5^{+7.9}_{-3.9}) \cdot 10^{-2}$	1.72
7.3–7.8	532	0.07	$(44.3 \pm 2.5^{+6.3}_{-3.0}) \cdot 10^{-2}$	1.67
7.8–8.4	1425	0.09	$(34.1 \pm 1.3^{+4.6}_{-2.3}) \cdot 10^{-2}$	1.6
8.4–9.0	2777	0.11	$(264 \pm 8.0^{+35}_{-18}) \cdot 10^{-3}$	1.56
9.0–9.7	3885	0.08	$(226 \pm 5.6^{+29}_{-15}) \cdot 10^{-3}$	1.51
9.7–10.6	5648	0.09	$(171 \pm 3.7^{+22}_{-11}) \cdot 10^{-3}$	1.46
10.6–11.5	5300	0.10	$(131 \pm 3.0^{+16}_{-8}) \cdot 10^{-3}$	1.42
11.5–12.4	4409	0.08	$(101 \pm 2.3^{+12}_{-6}) \cdot 10^{-3}$	1.42
12.4–13.5	6742	0.08	$(75.8 \pm 1.5^{+8.6}_{-4.4}) \cdot 10^{-3}$	1.28
13.5–14.6	5880	0.07	$(62.3 \pm 1.3^{+6.8}_{-3.4}) \cdot 10^{-3}$	1.28
14.6–15.8	9857	0.08	$(457 \pm 8.3^{+48}_{-25}) \cdot 10^{-4}$	1.14
15.8–17.2	8527	0.09	$(363 \pm 7.0^{+37}_{-20}) \cdot 10^{-4}$	1.14
17.2–18.6	7189	0.07	$(281 \pm 5.5^{+27}_{-14}) \cdot 10^{-4}$	1.14
18.6–20.2	6102	0.10	$(217 \pm 4.7^{+21}_{-11}) \cdot 10^{-4}$	1.14
20.2–21.9	9361	0.10	$(168 \pm 3.2^{+15}_{-8}) \cdot 10^{-4}$	1.0
21.9–23.8	7883	0.10	$(132 \pm 2.7^{+11}_{-6}) \cdot 10^{-4}$	1.0
23.8–25.8	6639	0.10	$(105.2 \pm 2.2^{+8.6}_{-4.8}) \cdot 10^{-4}$	1.0
25.8–28.0	5674	0.12	$(80.4 \pm 1.9^{+6.4}_{-4.0}) \cdot 10^{-4}$	1.0
28.0–30.4	4781	0.10	$(63.3 \pm 1.5^{+4.7}_{-2.8}) \cdot 10^{-4}$	1.0
30.4–32.9	4234	0.11	$(52.5 \pm 1.3^{+3.7}_{-2.3}) \cdot 10^{-4}$	1.0
32.9–35.7	3411	0.13	$(38.7 \pm 1.1^{+2.6}_{-1.8}) \cdot 10^{-4}$	1.0
35.7–38.8	2899	0.13	$(297 \pm 9.3^{+19}_{-13}) \cdot 10^{-5}$	1.0
38.8–43.1	2948	0.14	$(222 \pm 6.9^{+14}_{-9}) \cdot 10^{-5}$	1.0
43.1–48.0	2325	0.16	$(153.7 \pm 5.6^{+9.3}_{-7.4}) \cdot 10^{-5}$	1.0
48.0–53.7	1955	0.17	$(113.9 \pm 4.5^{+6.5}_{-6.5}) \cdot 10^{-5}$	1.0
53.7–60.4	1527	0.14	$(79.6 \pm 3.3^{+3.8}_{-3.9}) \cdot 10^{-5}$	1.0
60.4–68.2	1172	0.15	$(53.8 \pm 2.6^{+2.7}_{-2.6}) \cdot 10^{-5}$	1.0
68.2–77.4	901	0.18	$(35.7 \pm 2.1^{+2.1}_{-1.5}) \cdot 10^{-5}$	1.0

Numerical values are given in Table I for LE and in Table II for HE events. Note that the LE part of the spectrum has poorer statistical precision due to the 1:250 on-board prescale. Figure 21 shows the LAT spectrum along with other recent experiments and with a CR propagation model based on pre-Fermi data [32].

The CR electron spectrum reported in this paper and shown in Fig. 21 is essentially the same as that published in [2] for the energy above 20 GeV, but with twice the data volume. Within the systematic errors (shown by the gray band in Fig. 21) the entire spectrum from 7 GeV to 1 TeV can be fitted by a power law with spectral index in the interval 3.03–3.13 (best fit 3.08), similar to that given in [2]. The spectrum is significantly harder (flatter) than that reported by previous experiments. The cross-check analysis using events with long paths in the instrument confirms the absence of any evident feature in the $e^+ + e^-$ spectrum from 50 GeV to 1 TeV, as originally reported in [2].

Below ~ 50 GeV the electron spectrum is consistent with previous experiments and does not indicate any flattening at low energies. This may be compared with previous experiments that made measurements over the last solar cycle with an opposite polarity of the solar magnetic field (e.g. [19, 33]), and which indicate that a significant flattening occurs only below ~ 6 GeV.

To fit the high-energy part of the Fermi LAT spectrum and to agree with the HESS data, a conventional propagation model requires an injection power-law index $\alpha \simeq 2.5$ above ~ 4 GeV and a cutoff at ~ 2 TeV. However, while providing good agreement with the high-energy part of the spectrum, a model with a single power-law injection index fails to reproduce the low-energy data. To obtain an agreement with all the available data at low energies we need the injection spectrum $\alpha \sim 1.5 - 2.0$ below ~ 4 GeV and a modulation parameter in the range $\Phi = 400 - 600$ MV. The latter was set to match proton spectrum at low energy during the first year of Fermi LAT operation [34]. An example of such a calculation using GALPROP code [35] is shown in Fig. 22. This model includes spatial Kolmogorov diffusion with spectral index $\delta = 0.33$ and diffusive reacceleration characterized by an Alfvén speed $v_A = 30$ km/s; the halo height was 4 kpc. Energy losses by inverse Compton scattering and synchrotron radiation were computed as a function of energy and position. Secondary electrons and positrons from CR proton and helium interactions with interstellar gas make a significant contribution to the total leptons flux, especially at low energies. These secondary particle fluxes were computed for the same GALPROP model as for the primary electrons as described in [12] and references therein. This model is essentially a conventional one with distributed reacceleration, described in [36]. For more information on CR and their propagation in the interstellar medium see e.g. a recent review [37].

We note that the force-field treatment [38], used in our calculation to evaluate the effect of solar modulation, is approximate and does not take into account many important effects, such as the configuration of the heliospheric

magnetic field and drift effects which lead to the charge-sign dependence (e.g. [39–41]). In addition, the value of the modulation potential Φ depends on the assumed interstellar particle spectra, and thus other combinations of parameters are also possible. Ultimately the interstellar spectrum of CREs can be tested using the LAT observations of the Galactic diffuse gamma-ray emission where the inverse Compton component is dominating the gas component at medium to high Galactic latitudes [42].

The Fermi LAT measured spectrum suggests some spectral flattening at 70–200 GeV and a noticeable excess above 200 GeV as compared to our power-law spectral fit. These gentle features of the spectrum can be explained within a conventional model by adjusting the injection spectra.

Another possibility that provides a good overall agreement with our spectrum is the introduction of an additional leptonic component with a hard spectrum (Fig. 23). Such an additional component is motivated by the rise in the positron fraction reported by PAMELA [11]. Recent papers have suggested different models for this component. The data can accommodate a contribution from nearby sources (such as pulsars) or from the annihilation of dark

TABLE II: Number of events, residual hadronic contamination and flux J_E for HE analysis. Statistical error is followed by systematic error (see Sec. III D). Residual contamination is defined as the ratio between hadronic background rate and measured event rate.

Energy (GeV)	Counts	Residual contamination	J_E ($\text{GeV}^{-1} \text{ s}^{-1} \text{ m}^{-2} \text{ sr}^{-1}$)
23.6–26.0	944 264	0.04	$(1020 \pm 1.2^{+50}_{-54}) \cdot 10^{-5}$
26.0–28.7	958 983	0.05	$(735 \pm 0.9^{+30}_{-33}) \cdot 10^{-5}$
28.7–31.7	967 571	0.05	$(566 \pm 0.6^{+20}_{-22}) \cdot 10^{-5}$
31.7–35.0	880 243	0.06	$(420 \pm 0.5^{+13}_{-16}) \cdot 10^{-5}$
35.0–38.8	754 385	0.08	$(302 \pm 0.4^{+9}_{-11}) \cdot 10^{-5}$
38.8–43.1	638 368	0.09	$(2180 \pm 3.0^{+71}_{-83}) \cdot 10^{-6}$
43.1–48.0	534 109	0.10	$(1577 \pm 2.4^{+55}_{-65}) \cdot 10^{-6}$
48.0–53.7	447 219	0.11	$(1110 \pm 1.9^{+38}_{-46}) \cdot 10^{-6}$
53.7–60.4	371 444	0.12	$(775 \pm 1.4^{+29}_{-38}) \cdot 10^{-6}$
60.4–68.2	297 616	0.13	$(536 \pm 1.1^{+21}_{-24}) \cdot 10^{-6}$
68.2–77.4	241 956	0.14	$(365 \pm 0.9^{+14}_{-19}) \cdot 10^{-6}$
77.4–88.1	191 926	0.15	$(247 \pm 0.7^{+11}_{-12}) \cdot 10^{-6}$
88.1–101	148 899	0.16	$(1659 \pm 5.1^{+77}_{-84}) \cdot 10^{-7}$
101–116	118 212	0.16	$(1097 \pm 3.8^{+52}_{-59}) \cdot 10^{-7}$
116–133	89 641	0.17	$(725 \pm 2.9^{+37}_{-38}) \cdot 10^{-7}$
133–154	67 146	0.18	$(470 \pm 2.2^{+25}_{-25}) \cdot 10^{-7}$
154–180	52 453	0.17	$(303 \pm 1.6^{+15}_{-16}) \cdot 10^{-7}$
180–210	37 352	0.18	$(192 \pm 1.2^{+10}_{-10}) \cdot 10^{-7}$
210–246	26 807	0.19	$(1198 \pm 9.0^{+68}_{-62}) \cdot 10^{-8}$
246–291	19 150	0.19	$(728 \pm 6.5^{+41}_{-37}) \cdot 10^{-8}$
291–346	13 648	0.19	$(434 \pm 4.6^{+23}_{-24}) \cdot 10^{-8}$
346–415	9183	0.19	$(251 \pm 3.2^{+14}_{-14}) \cdot 10^{-8}$
415–503	5845	0.19	$(1407 \pm 22^{+95}_{-92}) \cdot 10^{-9}$
503–615	3577	0.20	$(754 \pm 15^{+56}_{-57}) \cdot 10^{-9}$
615–772	2092	0.19	$(370 \pm 10^{+54}_{-39}) \cdot 10^{-9}$
772–1000	1039	0.20	$(179 \pm 6.9^{+32}_{-25}) \cdot 10^{-9}$

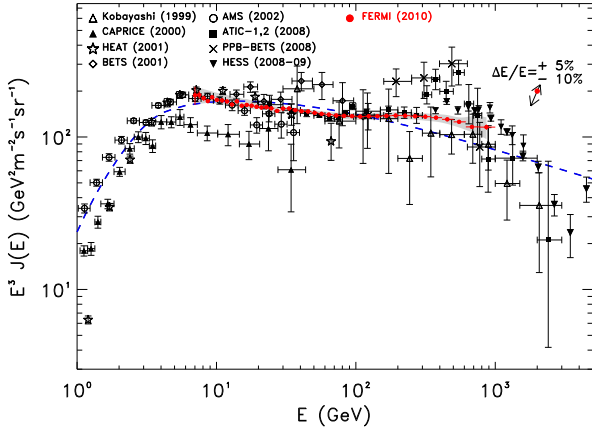


FIG. 21: (color). Cosmic-ray electron spectrum as measured by Fermi LAT for 1 yr of observations - shown by filled circles, along with other recent high-energy results. The LE spectrum is used to extend the HE analysis at low energy. Systematic errors are shown by the gray band. The range of the spectrum rigid shift implied by a shift of the absolute energy is shown by the arrow in the upper right corner. Dashed line shows the model based on pre-Fermi results [32]. Data from other experiments are: Kobayashi [45], CAPRICE [33], HEAT [46], BETS [47], AMS [19], ATIC [7], PPB-BETS [8], and HESS [9, 10]. Note that the AMS and CAPRICE data are for e^- only.

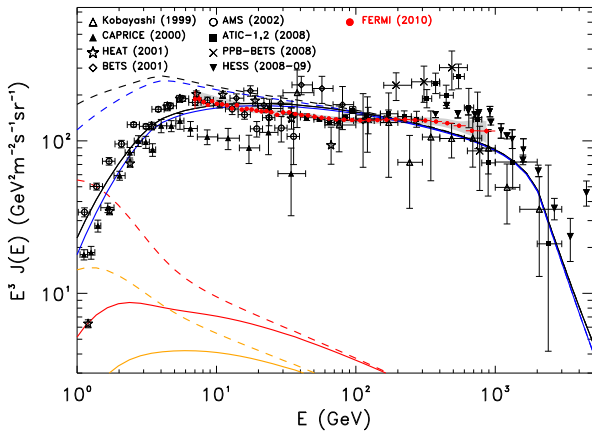


FIG. 22: (color). The $e^+ + e^-$ spectrum computed with the conventional GALPROP model [36] (shown by solid black line) is compared with the Fermi LAT (red filled circles) and other experimental data. This model adopts an injection spectral index $\Gamma = 1.6/2.5$ below/above 4 GeV, and a steepening $\Gamma = 5$ above 2 TeV. Blue lines show e^- spectrum only. The solar modulation was treated using the force-field approximation with $\Phi = 550$ MV. The dashed/solid lines show the before modulation/modulated spectra. Secondary e^+ (red lines) and e^- (orange lines) are calculated using the formalism from [12].

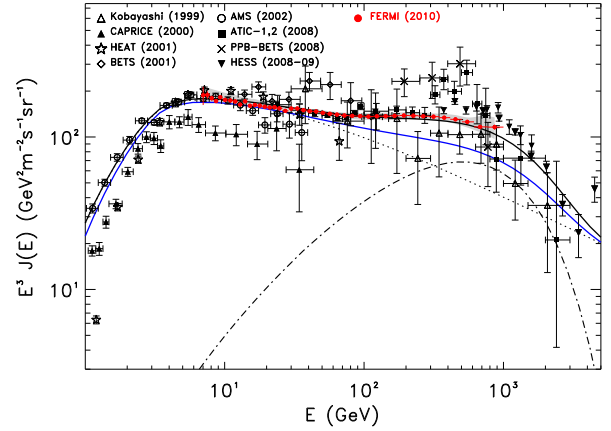


FIG. 23: (color). The $e^+ + e^-$ spectrum (solid line) computed with the conventional GALPROP model [36] but with a different injection spectrum: an injection index $\Gamma = 1.6/2.7$ below/above 4 GeV (dotted line). An additional component with an injection index $\Gamma = 1.5$ and exponential cutoff is shown by the dashed line. Blue line shows e^- spectrum only. Secondary e^+ and e^- are treated as in Fig. 22. Fermi-LAT data points are shown by red filled circles.

matter particles (see e.g. [14] for a comprehensive list of references). The features may also be explained by other astrophysical effects ([43, 44] and others). Further discussion of these many models, as well as an interpretation of low-energy data with more realistic models for heliospheric propagation, is beyond the scope of this paper.

Acknowledgments

The Fermi LAT Collaboration acknowledges generous ongoing support from a number of agencies and institutes that have supported both the development and the operation of the LAT as well as scientific data analysis. These include the National Aeronautics and Space Administration and the Department of Energy in the United States; the Commissariat à l'Énergie Atomique and the Centre National de la Recherche Scientifique/Institut National de Physique Nucléaire et de Physique des Particules in France; the Agenzia Spaziale Italiana and the Istituto Nazionale di Fisica Nucleare in Italy; the Ministry of Education, Culture, Sports, Science, and Technology (MEXT), High Energy Accelerator Research Organization (KEK), and Japan Aerospace Exploration Agency (JAXA) in Japan; and the K. A. Wallenberg Foundation, the Swedish Research Council, and the Swedish National Space Board in Sweden. Additional support for science analysis during the operations phase is gratefully acknowledged from the Istituto Nazionale di Astrofisica in Italy and the Centre National d'Études Spatiales in France. We would like to thank the INFN GRID Data Centers of Pisa, Trieste, and CNAF-Bologna;

the DOE SLAC National Accelerator Laboratory Computing Division and the CNRS/IN2P3 Computing Center (CC-IN2P3—Lyon/Villeurbanne) in partnership with CEA/DSM/Irfu for their strong support in performing the massive simulations necessary for this work. J. Conrad is

Fellow of the Royal Swedish Academy of Sciences, funded by a grant from the K. A. Wallenberg Foundation. L. Tibaldo is partially supported by the International Doctorate on Astroparticle Physics (IDAPP) program.

-
- [1] W. B. Atwood, A. A. Abdo, M. Ackermann, W. Alt-house, B. Anderson, M. Axelsson, L. Baldini, J. Ballet, D. L. Band, G. Barbiellini, et al., *Astrophys. J.* **697**, 1071 (2009).
- [2] A. A. Abdo, M. Ackermann, M. Ajello, W. B. Atwood, M. Axelsson, L. Baldini, J. Ballet, G. Barbiellini, D. Bastieri, M. Battelino, et al., *Phys. Rev. Lett.* **102**, 181101 (2009).
- [3] J. Nishimura, M. Fujii, T. Taira, E. Aizu, H. Hiraiwa, T. Kobayashi, K. Niu, I. Ohta, R. L. Golden, and T. A. Koss, *Astrophys. J.* **238**, 394 (1980).
- [4] S. W. Barwick, J. J. Beatty, C. R. Bower, C. J. Chaput, S. Coutu, G. A. de Nolfo, M. A. DuVernois, et al., *Astrophys. J.* **498**, 779 (1998).
- [5] D. Müller, *Adv. Space Res.* **27**, 659 (2001).
- [6] F. A. Aharonian, A. M. Atoyan, and H. J. Voelk, *Astron. Astrophys.* **294**, L41 (1995).
- [7] J. Chang, J. H. Adams, H. S. Ahn, G. L. Bashindzhagyan, M. Christl, O. Ganel, T. G. Guzik, J. Isbert, K. C. Kim, E. N. Kuznetsov, et al., *Nature (London)* **456**, 362 (2008).
- [8] S. Torii, T. Yamagami, T. Tamura, K. Yoshida, H. Kitamura, K. Anraku, J. Chang, M. Ejiri, I. Iijima, A. Kadokura, et al., arXiv:0809.0760.
- [9] F. Aharonian, A. G. Akhperjanian, U. Barres de Almeida, A. R. Bazer-Bachi, Y. Becherini, B. Behera, W. Benbow, K. Bernlöhr, C. Boisson, A. Bochow, et al., *Phys. Rev. Lett.* **101**, 261104 (2008).
- [10] F. Aharonian, A. G. Akhperjanian, G. Anton, U. Barres de Almeida, A. R. Bazer-Bachi, Y. Becherini, B. Behera, K. Bernlöhr, A. Bochow, C. Boisson, et al., *Astron. Astrophys.* **508**, 561 (2009).
- [11] O. Adriani, G. C. Barbarino, G. A. Bazilevskaya, R. Bellotti, M. Boezio, E. A. Bogomolov, L. Bonechi, M. Bongì, V. Bonvicini, S. Bottai, et al., *Nature (London)* **458**, 607 (2009).
- [12] I. V. Moskalenko and A. W. Strong, *Astrophys. J.* **493**, 694 (1998).
- [13] T. Kobayashi, Y. Komori, K. Yoshida, and J. Nishimura, *Astrophys. J.* **601**, 340 (2004).
- [14] D. Grasso, S. Profumo, A. W. Strong, L. Baldini, R. Bellazzini, E. D. Bloom, J. Bregeon, G. di Bernardo, D. Gaggero, N. Giglietto, et al., *Astropart. Phys.* **32**, 140 (2009).
- [15] J. F. Ormes et al., in *Proceedings of the 25th International Cosmic Ray Conference*, edited by M. S. Potgieter, C. Raubenheimer, and D. J. van der Walt (Potchefstroom University, Transvaal, South Africa, 1997), vol. 5, pp. 73.
- [16] A. A. Moiseev, J. F. Ormes, and I. V. Moskalenko, in *Proceedings of the 30th International Cosmic Ray Conference*, edited by Rogelio Caballero, Juan Carlos D’Olivo, Gustavo Medina-Tanco, Lukas Nellen, Federico A. Sánchez, José F. Valdés-Galicia (Universidad Nacional Autónoma de México, Mexico City, Mexico, 2008), vol. 2, pp. 449, arXiv:astro-ph/0706.0882.
- [17] L. Baldini, A. Brez, T. Himel, M. Hirayama, R. P. Johnson, W. Kroeger, L. Latronico, M. Minuti, D. Nelson, R. Rando, et al., *IEEE Trans. Nucl. Sci.* **53**, 466 (2006).
- [18] A. A. Abdo, M. Ackermann, M. Ajello, J. Ampe, B. Anderson, W. B. Atwood, M. Axelsson, R. Bagagli, L. Baldini, J. Ballet, et al., *Astropart. Phys.* **32**, 193 (2009).
- [19] M. Aguilar, J. Alcaraz, J. Allaby, B. Alpat, G. Ambrosi, H. Anderhub, L. Ao, A. Arefiev, P. Azzarello, et al., (AMS Collaboration), *Phys. Rep.* **366**, 331 (2002).
- [20] S. Haino, T. Sanuki, K. Abe, K. Anraku, Y. Asaoka, H. Fuke, M. Imori, A. Itasaki, T. Maeno, Y. Makida, et al., *Phys. Lett. B* **594**, 35 (2004).
- [21] S. Agostinelli, J. Allison, K. Amako, J. Apostolakis, H. Araujo, P. Arce, M. Asai, D. Axen, S. Banerjee, G. Bartrand, et al., *Nucl. Instrum. Methods Phys. Res., Sect. A* **506**, 250 (2003).
- [22] C. Sgrò, J. Bregeon, L. Baldini (for the Fermi LAT collaboration), in *Proceedings of 31st International Cosmic Ray Conference* Łódź, Poland, 2009, arXiv:0907.0385.
- [23] P. Zuccon, B. Bertucci, B. Alpat, G. Ambrosi, R. Battiston, G. Battistoni, W. J. Burger, D. Caraffini, C. Cecchi, L. di Masso, et al., *Astropart. Phys.* **20**, 221 (2003).
- [24] L. Baldini, G. Barbiellini, R. Bellazzini, J. R. Bogart, G. Bogaert, E. Bonamente, J. Bregeon, A. Brez, M. Brigida, A. W. Borgland, et al., in *The First GLAST Symposium*, edited by S. Ritz, P. Michelson, & C. A. Meehan (2007), vol. 921 of *American Institute of Physics Conference Series*, pp. 190–204.
- [25] K. Nakamura et al., *J. Phys. G* **37**, 075021 (2010), URL <http://pdg.lbl.gov>.
- [26] A. Heikkinen, in *The Monte Carlo Method: Versatility Unbounded in a Dynamic Computing World* (American Nuclear Society, 2005).
- [27] GEANT4 Collaboration, GEANT4 Physics List, URL http://geant4.cern.ch/support/proc_mod_catalog/physics_lists/physicsLists.shtml.
- [28] N. M. Ball and R. J. Brunner, *Int. J. Mod. Phys. D*, **19**, 1049, (2010), arXiv:0906.2173.
- [29] G. D’Agostini, *Nucl. Instrum. Methods Phys. Res., Sect. A* **362**, 487 (1995).
- [30] D. F. Smart and M. A. Shea, *Adv. Space Res.* **36**, 2012 (2005).
- [31] International Association of Geomagnetism and Aeronomy, International Geomagnetic Reference Field, URL <http://www.ngdc.noaa.gov/IAGA/vmod/igrf.html>.
- [32] A. W. Strong, I. V. Moskalenko, and O. Reimer, *Astrophys. J.* **613**, 962 (2004).
- [33] M. Boezio, P. Carlson, T. Francke, N. Weber, M. Suffert, M. Hof, W. Menn, M. Simon, S. A. Stephens, R. Bellotti, et al., *Astrophys. J.* **532**, 653 (2000).
- [34] M. Casolino, N. de Simone, M. P. de Pascale, V. di Felice, L. Marcelli, M. Minori, P. Picozza, R. Sparvoli, G. Castellini, O. Adriani, et al., *Nucl. Phys. B, Proc. Suppl.* **190**, 293 (2009).
- [35] A. W. Strong and I. V. Moskalenko, *Astrophys. J.* **509**,

- 212 (1998).
- [36] V. S. Ptuskin, I. V. Moskalenko, F. C. Jones, A. W. Strong, and V. N. Zirakashvili, *Astrophys. J.* **642**, 902 (2006).
- [37] A. W. Strong, I. V. Moskalenko, and V. S. Ptuskin, *Annual Review of Nuclear and Particle Science* **57**, 285 (2007).
- [38] L. J. Gleeson and W. I. Axford, *Astrophys. J.* **154**, 1011 (1968).
- [39] J. Clem and P. Evenson, *Journal of Geophysical Research (Space Physics)* **114**, 10108 (2009).
- [40] S. E. S. Ferreira and M. S. Potgieter, *Astrophys. J.* **603**, 744 (2004).
- [41] M. S. Potgieter, *Adv. Space Res.* **19**, 883 (1997).
- [42] A. A. Abdo, M. Ackermann, M. Ajello, B. Anderson, W. B. Atwood, M. Axelsson, L. Baldini, J. Ballet, G. Barbiellini, D. Bastieri, et al., *Phys. Rev. Lett.* **103**, 251101 (2009).
- [43] L. Stawarz, V. Petrosian, and R. D. Blandford, *Astrophys. J.* **710**, 236 (2010).
- [44] P. Blasi, *Phys. Rev. Lett.* **103**, 051104 (2009).
- [45] T. Kobayashi et al., in *Proceedings of the 26th International Cosmic Ray Conference, Salt Lake City*, 1999, URL <http://adsabs.harvard.edu/abs/1999ICRC...3...61K>
- [46] M. A. DuVernois, S. W. Barwick, J. J. Beatty, A. Bhattacharyya, C. R. Bower, C. J. Chaput, S. Coutu, G. A. de Nolfo, D. M. Lowder, S. McKee, et al., *Astrophys. J.* **559**, 296 (2001).
- [47] S. Torii, T. Tamura, N. Tateyama, K. Yoshida, J. Nishimura, T. Yamagami, H. Murakami, T. Kobayashi, Y. Komori, K. Kasahara, et al., *Astrophys. J.* **559**, 973 (2001).